Lucas Soares Gusman

Design for Reliability of Multifunctional PV Inverters used in Industrial Power Factor Regulation

Belo Horizonte, MG

2020

Lucas Soares Gusman

Design for Reliability of Multifunctional PV Inverters used in Industrial Power Factor Regulation

Dissertação submetida à banca examinadora designada pelo Colegiado do Programa de Pós-Graduação em Engenharia Elétrica do Centro Federal de Educação Tecnológica de Minas Gerais e da Universidade Federal de São João Del Rei, como parte dos requisitos necessários à obtenção do grau de Mestre em Engenharia Elétrica.

Centro Federal de Educação Tecnológica de Minas Gerais

Programa de Pós-Graduação em Engenharia Elétrica

Orientador: Prof. Dr. Heverton Augusto Pereira

Coorientador: Prof. Dr. Allan Fagner Cupertino

Belo Horizonte, MG

2020

Lucas Soares Gusman
Design for Reliability of Multifunctional PV Inverters used in Industrial Power Factor Regulation/ Lucas Soares Gusman. – Belo Horizonte, MG, 2020-
83 p.

Orientador: Prof. Dr. Heverton Augusto Pereira
Coorientador: Prof. Dr. Allan Fagner Cupertino

– Centro Federal de Educação Tecnológica de Minas Gerais
Programa de Pós-Graduação em Engenharia Elétrica, 2020.

1. Multifunctional PV Inverter. 2. Power Factor Regulation. 3. Capacitor Banks. 4. Lifetime Evaluation. 5. Industries 6. Economical Evaluation. I. Orientador: Heverton Augusto Pereira. II. Coorientador: Allan Fagner Cupertino. III. Centro Federal de Educação Tecnológica de Minas Gerais. IV. Pós Graduação em Engenharia Elétrica. V. Design for Reliability of Multifunctional PV Inverters used in Industrial Power Factor Regulation

UNIVERSIDADE FEDERAL DE SÃO JOÃO DEL REI
PRÓ-REITORIA DE PESQUISA E PÓS-GRADUAÇÃO

CENTRO FEDERAL DE EDUCAÇÃO TECNOLÓGICA DE MINAS GERAIS
DIRETORIA DE PESQUISA E PÓS-GRADUAÇÃO

PROGRAMA DE PÓS-GRADUAÇÃO EM ENGENHARIA ELÉTRICA

Lucas Soares Gusman

"Design for Reliability of Multifunctional PV Inverters used in Industrial Power Factor Regulation"

Dissertação nº 244 apresentada ao Programa de Pós-Graduação em Engenharia Elétrica – Associação Ampla entre a Universidade Federal de São João Del-Rei e o Centro Federal de Educação Tecnológica de Minas Gerais em 05 de Novembro de 2020 como requisito parcial para obtenção do título de Mestre em Engenharia Elétrica, aprovada pela Banca Examinadora constituída pelos professores:

Heverton Augusto Pereira
____
Prof. Dr. Heverton Augusto Pereira (Orientador)
Universidade Federal de Viçosa

Allan Fagner Cupertino
____
Prof. Dr. Allan Fagner Cupertino (Coorientador)
Centro Federal de Educação Tecnológica de Minas Gerais

Wesley Peres
____
Prof. Dr. Wesley Peres
Universidade Federal de São João del-Rei – UFSJ

Hélio Marcos André Antunes
____
Prof. Dr. Hélio Marcos André Antunes
Universidade Federal do Espírito Santo – UFES

À minha família, mentores e amigos.

Agradecimentos

Agradeço de coração a todos que fizeram parte dessa jornada e que, direta ou indiretamente, me deram forças e apoio durante o desenvolvimento desse mestrado. É imprescindível reforçar o quanto de conhecimento é adquirido ao longo de uma jornada como essa, tanto por amigos, família e mentores, o que sem dúvidas me fez uma pessoa melhor.

Agradeço aos meus pais Silvia e Marcelo, por todo apoio que recebo desde o início da minha vida. Por estarem lá quando tudo parece extremamente difícil e me ajudarem a seguir em frente a fim de conseguir uma vida melhor.

Agradeço à minha irmã e meu cunhado Grasi e Alan, por estarem sempre ao meu lado em Viçosa, me oferecendo todo apoio do mundo. Apoio e fins de semana divertidos e cheios de trabalhos braçais disfarçados de jogos! Além disso, devo dedicar ao meu recém sobrinho/afiliado Murilo, a quem eu amo de coração e dedicarei parte da minha vida a cuidar e zelar.

Agradeço à minha namorada Daiane por sempre estar ao meu lado em todas decisões, mesmo que estejamos longe às vezes. Uma pessoa que sempre esteve ao meu lado nos momentos bons e ruins também, me dando todo tipo de força para seguir em frente.

Agradeço ao meu orientador Heverton e ao meu coorientador Allan, os quais compartilharam todo conhecimento e projetos possíveis comigo. Além da ajuda em ler exaustivamente este texto a fim de melhora-lo! Agradeço ainda ao CEFET-MG pela oportunidade de realizar este processo de mestrado em uma instituição incrível.

Por fim, agradeço a todos meus amigos e principalmente os do GESEP: João Marcus, William, Dayane e Paulo Júnior, os quais seguiram firmes esse caminho comigo desde o início da graduação. Ainda que nossos caminhos se separem, a recordação de todos os momentos de diversão e aprendizagem vão se manter eternamente.

“Dream until your dreams come true.”
Aerosmith

Resumo

Consumidores industriais são conhecidos por sua alta demanda de potência ativa e reativa. Assim, tais consumidores possuem grande interesse na geração local por meio de usinas fotovoltaicas (FV) para redução das contas de energia. No entanto, os sistemas FV tradicionais reduzem a potência ativa absorvida da rede e, consequentemente, o fator de potência da instalação. Sob tais condições, multas são cobradas por baixo fator de potência na instalação. Este trabalho realiza um estudo dos efeitos da instalação de uma planta FV no fator de potência industrial. Além disso, soluções baseadas na correção usando bancos de capacitores tradicionais e em inversores FV multifuncionais são implementadas. O estudo de caso de uma planta industrial localizada no Brasil é discutido. Os resultados indicam que o banco de capacitores tradicional é incapaz de corrigir o fator de potência precisamente pelo seu número limitado de taps. De fato, os inversores FV multifuncionais podem prover compensação de potência reativa precisa, o que melhora o fator de potência e elimina multas adicionais. No entanto, uma redução de 24,1 % na vida útil do inversor fotovoltaico é observada em comparação à operação tradicional. Desta forma, uma proposta de dimensionamento do inversor é apresentada com a finalidade de preservar a confiabilidade do sistema considerando a funcionalidade extra do inversor FV (correção de fator de potência).

Palavras-chaves: Indústrias; Inversores Fotovoltaicos Multifuncionais; Correção de Fator de Potência; Análise de Confiabilidade; Avaliação Econômica.

Abstract

Industrial consumers are widely known for their high demand for active and reactive power. Thus, these consumers have a great interest in the local generation using PV plants to reduce the energy bill. However, the traditional PV systems reduce the active power absorbed from the grid and, consequently, the installation power factor. Under such conditions, fees are being charged due to the low power factor value. This work carries out an overall study on the effects of the installation of a PV plant on the industrial power factor. Moreover, a benchmarking of traditional capacitor banks and the multifunctional PV inverter is performed. The case study of an industrial power plant located in Brazil is discussed. The results indicate that the traditional capacitor bank solution cannot correct the power factor all time due to its limited number of taps. Nevertheless, the multifunctional PV inverter can provide a precise reactive power compensation, which improves the power factor and reduces the additional fees. Finally, a PV system reliability reduction of 24.1 % is observed compared to the traditional operation, while inverter oversizing preserves the system reliability even if multifunctional operation is assumed.

Key-words: Industries; Multifunctional PV inverter; Power Factor Correction; Reliability Analysis; Economical Evaluation.

List of Figures

List of Tables

List of abbreviations and acronyms

Al-Caps	Aluminum Electrolytic Capacitors
CDF	Cumulative Density Function
DSOGI	Dual Second-Order Generalized Integrator
DSP	Digital Signal Processor
ESL	Equivalent Series Inductance
ESR	Equivalent Series Resistance
FFT	Fast Fourier Transform
FV	Fotovoltaica
IGBT	Insulated Gate Bipolar Transistor
LC'	Lifetime Consumption
LVRT	Low-Voltage Ride Through
MOSFET	Metal Oxide Silicon Field Effect Transistor
MP	Mission Profile
MPPT	Maximum Power Point Tracking
PDF	Probability Density Function
PF	Power Factor
PI	Proportional-Integral
PLL	Phase-Locked Loop
PoF	Physics of Failure
PSC	Positive Sequence Calculator
PV	Photovoltaic
PWM	Pulse Width Modulation
QSG	Quadrature Signal Generator

RMS	Root Mean Square
SOGI	Second-Order Generalized Integrator
SVPWM	Space Vector Pulse Width Modulation
SRF	Synchronous Reference Frame
THD	Total Harmonic Distortion
VSI	Voltage Source Inverter

List of symbols

P	Three-Phase Active Power
V_ϕ	Phase-to-Phase Voltage
ϕ	Angle of the Phase Impedance
μ	Base Energy Tax
E_G	Consumed Active Energy
PF_{ref}	Threshold Value for the Power Factor
p	Total of Hours for Measurement
Q_C	Capacitive Reactive Power
Q_L	Inductive Reactive Power Consumed by the Load
P_L	Active Power Consumed by the Load
PF^*	Reference Power Factor
v_{dc}	dc-link Voltage
v_{gabc}	Grid Voltage in abc Reference
i_{gabc}	Grid Current in abc Reference
Q^*	Reactive Power Reference for the Control
P^*_{INV}	Active Power Reference for the Inverter
Q^*_{INV}	Reactive Power Reference for the Inverter
$P^{*'}_{INV}$	Saturated Active Power for the Inverter
$Q^{*'}_{INV}$	Saturated Reactive Power for the Inverter
v_{gd}	Grid Voltage in the Direct Axis
v_{gq}	Grid Voltage in the Quadrature Axis
i_{gd}	Grid Current in the Direct Axis
i_{gq}	Grid Current in the Quadrature Axis

ω	Grid Angular Frequency
L	LCL Filter Total Inductance
ρ	Phase Angle of the Grid Voltage
PWM_{inv}	PWM Reference for the Inverter
P_{INV}	Active Power Delivered by the Inverter
Q_{INV}	Reactive Power Delivered by the Inverter
S_n	Inverter Rated Power
P_G	Active Power Drawn from the Grid
PF_{PV}	Power Factor with the Installation of a PV Plant
N_{tap}	Number of Taps for the Capacitor Bank
$Q_{C,T}$	Capacitive Reactive Power Rounded to a Number of Taps
ΔQ_C	Step Size of One Tap
k	Oversizing Factor for the Inverter
PF_{CAP}	Power Factor Corrected by the Tapped Capacitor Bank
PF_{INV}	Power Factor Corrected by the Inverter
PF_i	Instantaneous Power Factor at Time i
C_{dc}	Dc-Link Capacitor
S_i	Gate Signal to the IGBT i in the Inverter
L_f	Inverter Side Filter Inductance
L_g	Grid Side Filter Inductance
R_f	Internal Resistance of the Inverter Side Inductance
R_g	Internal Resistance of the Grid Side Inductance
C_f	Filter Capacitance
r_d	Filter Damping Resistor
V_g	Grid Phase-to-Phase Voltage
I_g	Grid Current

v_α	Alpha-Coordinate Grid Voltage
v_β	Beta-Coordinate Grid Voltage
v'_α	Filtered Alpha-Coordinate Grid Voltage
qv'_α	Quadrature Filtered Alpha-Coordinate Grid Voltage
v'_β	Filtered Beta-Coordinate Grid Voltage
qv'_β	Quadrature Filtered Beta-Coordinate Grid Voltage
v^+_α	Positive Sequence Alpha-Coordinate Grid Voltage
v^+_β	Positive Sequence Beta-Coordinate Grid Voltage
$T_{\alpha\beta}$	Transformation Matrix from abc to $\alpha\beta$ Coordinates
T_{dq}	Transformation Matrix from $\alpha\beta$ to dq Coordinates
v^+_q	Positive Sequence Q-Coordinate Grid Voltage
θ'	Phase Angle of the Grid Voltage
$\Delta\epsilon_{pl}$	Strain Difference Between Elastic and Plastic Behavior
σ_{yield}	Limit Stress to Achieve Plastic Behavior
G	Solar Irradiance
T_a	Ambient Temperature
T_j	Junction Temperature
P_{loss}	Conduction plus Switching Losses for Semiconductors
$I_c(h)$	h-harmonic Capacitor Current
$i_{dc}(t)$	Dc-Link Current
$f(x)$	Probability Density Function (PDF)
$F(x)$	Cumulative Density Function (CDF) / Unreliability
B_x	Time which x % of the Samples Fail
P_{co}	Conduction Losses
P_{sw}	Switching Losses
P_c	Capacitor Losses

T_c	Case Temperature
R_{c-h}	Case-to-Heatsink Thermal Resistance
R_{h-a}	Heatsink-to-Ambient Thermal Resistance
T_h	Hotspot Temperature
R_{thc}	Hotspot-to-Case Thermal Resistance
C_{thc}	Hotspot-to-Case Thermal Capacitance
t_{on}	Heating Time
ΔT_j	Junction Temperature Fluctuation
T_{jm}	Average Junction Temperature
R_c	Hotspot-to-Ambient Equivalent Thermal Resistance
f_n	Fundamental Frequency
N_f	Number of Cycles to Failure
f_d	Semiconductor Parameter
L	Capacitor Lifetime Under Operating Conditions
L_0	Capacitor Lifetime Under Testing Conditions
V_0	Capacitor Voltage Under Testing Condition
T_0	Capacitor Temperature Under Testing Condition
n	Voltage Stress Exponent
$N_{f(l)_k}$	Number of Cycles to Failure for Each k Sample of the Long Cycle
$N_{f(s)_k}$	Number of Cycles to Failure for Each k Sample of the Short Cycle
T_s	Sample Time of the Mission Profile
t'_{on}	Static Heating Time
$\Delta T'_j$	Static Junction Temperature Fluctuation
T'_{jm}	Static Average Junction Temperature
$N_{f,i}$	Number of Cycles to Failure for the i Monte Carlo Simulation
$F_i(x)$	Unreliability of the IGBTs

$F_d(x)$	Unreliability of the Diodes
$F_c(x)$	Unreliability of the Capacitors
n_i	Number of IGBTs
n_d	Number of Diodes
n_c	Number of Capacitors
F_{sys}	System Unreliability
B_{10}	Time when 10 % of the Samples Fail
$\overline{G}$	Average Irradiance
A_p	Area of the Solar Panel
η	Efficiency of the Panel
N	Number of Panels
$E_{industry}$	Daily Energy Demanded by the Industry
E_{panel}	Daily Energy Produced by the PV Panel
P_{max}	PV Panel Rated Maximum Power
V_{mp}	PV Panel Maximum Power Voltage
I_{mp}	PV Panel Maximum Power Current
V_{oc}	PV Panel Open Circuit Voltage
I_{sc}	PV Panel Short Circuit Current
N_s	PV Panel Number of Cells
$K_{p,cur}$	Current Proportional Gain
$K_{i,cur}$	Current Integral Gain
$K_{p,bus}$	Bus Control Proportional Gain
$K_{i,bus}$	Bus Control Integral Gain
$K_{p,rea}$	Reactive Control Proportional Gain
$K_{i,rea}$	Reactive Control Integral Gain
R_{thi}	Foster Thermal Resistance for the i Layer

τ_i	Foster Thermal Time Constant for the i Layer
C_{thi}	Foster Thermal Capacitance for the i Layer

Contents

1 Introduction

1.1 Context and Relevance

Small, medium and large industries consider that the reduction of the energy provided by the electric utility is determining for the reduction of their fixed costs. Hence, investment in local photovoltaic (PV) solar generation has increased rapidly in recent decades, mainly in the industrial sector. Associated with reduced energy bill, PV systems attract great interest due to the production of sustainable energy with low environmental impact and reduced maintenance costs (Yang; Sangwongwanich; Blaabjerg, 2016). However, the increasing penetration of PV systems into the grid has made it more vulnerable, which has led the need for studies to assess their impacts (Wandhare; Agarwal, 2014).

Fig. 1 shows the increasing total installed capacity of PV power plants in Brazil. The growth of this type of energy has become more evident in the recent years, in a large scale for industrial applications. In the recent 4 years, the total increase on the installed PV power has grown higher than 320 %.

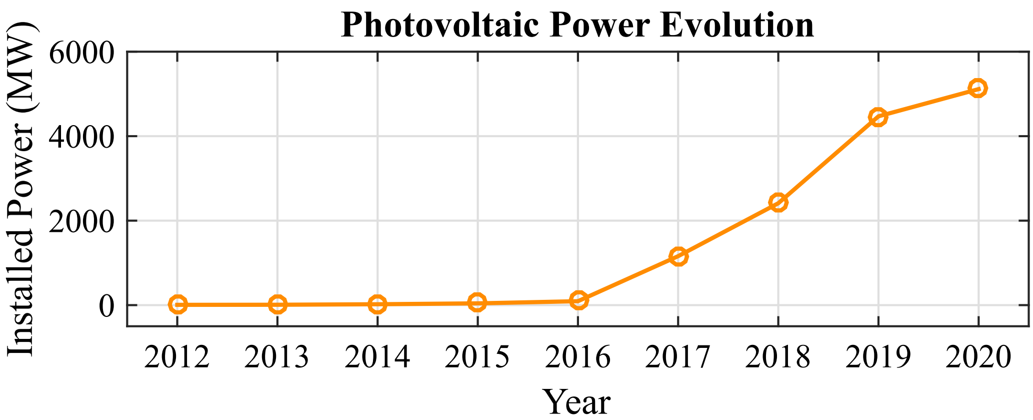

Figure 1 – Total installed capacity of PV power plants in Brazil. (Absolar, 2020)

The industry draws a certain amount of active and reactive power from the grid to supply the power demanded by its load. However, the introduction of a photovoltaic plant reduces the liquid active power demand from the grid due to local generation. According to the power triangle, reduction of active power results in an increased power factor (PF) angle. Therefore, it can reduce the PF to below the acceptable limit, according to the grid standards (ANEEL, 2010). The industry power factor must be corrected to above the threshold allowed by the standards, or else there will be extra fees over the exceeding reactive power (ANEEL, 2010). In this scenario, reactive power support to avoid paying fees due to low PF is essential to make the investment in the PV system attractive

(Bhattacharya; Zhong, 2001).

PF correction is often carried out by capacitor banks (Joksimovic, 2015; Ko; Gu; Lee, 2018). However, this is not a trivial task when the loads present great variation over the year (Prasai; Sastry; Divan, 2010). Some works present solutions based on dynamic capacitors controlled by thyristors, although these solutions inject a great amount of harmonics into the grid (Prasai; Divan, 2011; Ahmed; Alam, 2006). Also, capacitor banks can present harmonic resonance with the grid, higher weight and higher volume occupied.

The aforementioned limitations can be mitigated using the multifunctional PV inverter approach. PV systems based on power inverters can inject active and reactive power (Liu et al., 2015), since their power control loops allow the inverter to perform PF correction while they inject active power. The reactive power support (Kekatos et al., 2015; Gandhi et al., 2016) is provided by multifunctional inverters in electrical power systems and microgrids. Reference (Su; Masoum; Wolfs, 2014) analyzes the reactive power support to maintain system voltage within the limits allowed by the standards. The work carried out in (Weckx; Gonzalez; Driesen, 2014) optimizes the utilization of the active and reactive powers to regulate the grid voltage during voltage sags. Furthermore, (Ye et al., 2016) and (Morales-Paredes; Bonaldo; Pomilio, 2018) use an inverter with the only purpose of correcting the power factor by controlling the capacitive reactive power delivered. Besides, the works in (Lo; Lee; Wu, 2008) and (Jafarian et al., 2018) use additional control loops implemented in the PV inverter to compensate the required reactive power.

Although many works do not assess the reactive power support impact, there are tradeoffs involving this functionality. Increased inverter power loss due to reactive power injection is the first tradeoff, which reduces the active power output margin and increases the temperature of inverter components. The second tradeoff is related to increased wear-out on the inverter components, which affects their reliability (Gandhi et al., 2019). Regarding the latter one, previous studies show that inverters are the most fragile link in the entire PV system (Moore; Post, 2008) and the extra work-time of the multifunctional operation by means of reactive power support can further aggravate this condition.

1.2 Power Factor Grid Codes

The power factor (PF) is defined as the total proportion of active power in the total apparent power. It is limited between 0 for only reactive power and 1 for only active power available. In fact, when there is an available active power P, the total current flowing in the system is given by:

$$I = \frac{P}{\sqrt{3}V_{\phi}\cos(\phi)}, \tag{1.1}$$

where V_ϕ is the line-to-line voltage and $\cos(\phi)$ is the cosine of the impedance per phase, which is the system power factor. Low power factor implies in low cosine values which results in high line currents. This current needed has many negative effects: it increases the losses along the industry cables, demands increased cable sizes and increases the total industry bills for the same active power consumed.

When $\cos(\phi) = 1$ (unitary PF) the current achieve the lowest value possible for the same active power consumed, avoiding the aforementioned drawbacks. Many industries have great amount of electrical motors which need certain amount of reactive power meaning that, naturally, the PF in industrial environments are lower than 1. For this reason, the grid codes in Brazil establish a minimum power factor of 0.92, whose value can be different for each country. When the PF of an installation is instantly below this threshold, fees are charged for exceeding reactive power.

The power factor is charged hourly based on the tax for active energy (in R$/kWh) by means of Eq. 1.2 calculated through the instantaneous value of the PF and the consumed energy (ANEEL, 2010).

$$\text{Fee} = \mu \sum_{i=1}^{p} \left\{ E_G(i) \left[\frac{PF_{ref}}{PF(i)} - 1 \right] \right\}, \tag{1.2}$$

where μ is the base energy tax in \$ per kWh, E_G is the consumed energy from the grid in each hour (in kWh), PF_{ref} is the threshold limit (0.92 in Brazil), PF(i) is the actual power factor in each hour and p is the total of hours in the analyzed period. μ is considered as \$ 0.0807 per kWh, which is the green flag value considered for the electrical company CEMIG. Also, for the rest of this work, the 1 dollar is considered to be R$ 4,25. This equation is valid only for PF values smaller than 0.92; for higher values, the total charge at this moment is equal to zero.

In environments where it is not possible to measure PF instantaneously, the tax is calculated using the mean PF value within the period of measurement. Besides, the PF cannot be lower than 0.92 capacitive in the period from 11h30 pm to 06h30 am. In the complementary hours of the day, the PF must not be lower than 0.92 inductive in the normal functioning of the industries.

This Master Thesis shows how the implementation of a PV plant reduces the industry PF and discusses the possible further corrections to this problem, addressing the effects on fees, lifetime and total cost of the system.

1.3 Objectives and Contributions

The industries are interested in evaluating the impacts of the photovoltaic solar plant connection to find the optimal solution to correct the PF and avoid fees. This work evaluates two strategies for industries to correct PF after installing the PV plant: (1) traditional, through a capacitor bank; and (2) with the implementation of reactive power support functionality through the PV inverter. Thereby, the following contributions are provided in this Master Thesis:

- Theoretical modeling of power factor correction in the presence of PV plants;
- Comparison between retrofitted capacitor banks with taps and multifunctional PV inverters for PF correction;
- Design of the multifunctional PV inverter based on its reliability function to achieve a defined inverter lifetime target;
- Comparison of costs for investment and power losses with the changes on the PV inverter oversizing.

1.4 List of Publications

This Master Thesis produced the following published paper:

- Gusman, L. S. et al. Design for Reliability of Multifunctional PV Inverters used in Industrial Power Factor Regulation. International Journal of Electrical Power and Energy Systems (IJEPES), v. 119, p. 105932, 2020. ISSN 0142-0615.

Also, during this Graduation Program, the following paper was developed:

- Callegari, J. M. S. ; Gusman, L. S. ; et al. Detection of stressed electronic components in pv inverter using thermal imaging. IEEE Latin America, 2020. ISSN 1548-0992.

1.5 Master Thesis Outline

This Master Thesis is divided in the following 6 chapters:

- Chapter 2 describes the link between an industrial environment and a grid-connected PV system, highlighting the direct effects on power factor. It also includes the modeling for the plant and control strategies involved in this implementation;
- Chapter 3 shows the physics of failure for semiconductors and capacitors and describe the methodology for lifetime evaluation of power converters;
- Chapter 4 describes the case study used for the work, along with the figures of merit and the cost analysis made for the system;

- Chapter 5 addresses the results of the theoretical analysis and a practical implementation and results for the control strategy proposed;

- Chapter 6 indicates the closure of this Thesis, consisting of the conclusions and future works.

2 PV Plants in Industrial Systems

In this chapter, the integration between an industry and a PV system is highlighted, considering all components in this system. The capacitor banks are divided in fixed and automatic; the control of the multifunctional PV inverter is described, along with the proposed saturation structure for power factor correction; theoretical profiles are proposed to analyze the effects of the PV system in the industry power factor; At last, the corrections with an automatic capacitor bank and a PV inverter are demonstrated

2.1 Interconnection of a PV System to an Industrial Grid

Fig. 2 shows a typical grid-connected industrial system after a photovoltaic plant installation. The system consists of a three-phase grid-connected PV system, which provides active power in the traditional operating mode to supply industry demand and a capacitor bank for PF correction.

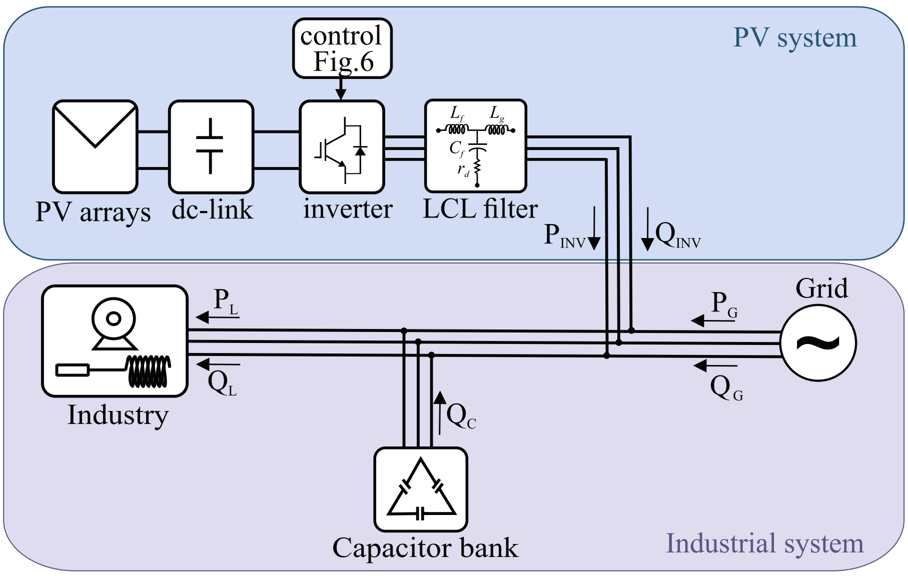

Figure 2 – Grid-connected industrial PV system.

The PV system is based on photovoltaic panels which generate energy collected from the solar irradiance. This energy is transferred to the dc-link and is injected into the grid by the inverter. A three-phase voltage source inverter (VSI) is considered in this work. This device can be based on IGBTs or MOSFETs, depending on the power and voltage ratings. The voltage output is a PWM modulated signal, which is then filtered by the LCL filter on the ac side of the converter. This process is a traditional operation of a grid connected inverter, following strict control strategies and grid codes to be commercially usable.

The industrial system is described as a RL load representing the sum of active and reactive power demanded from every machine and operating equipment within the factory. This kind of load is considered almost constant since it comes from the power rating from each equipment.

For its high demand of reactive power, industries are usually charged on the PF value as an exceeding reactive energy fee. The correction of this PF is often made with capacitor banks. These banks are normally constructed in delta configuration and are designed based on the line-to-line voltage and the required capacitive reactive power (in kvar) needed. Considering a constant active and reactive power for the load as P_L and Q_L, this capacitive power can be determined using:

$$Q_C = Q_L - P_L.\tan(\cos^{-1}(PF^*)), \tag{2.1}$$

where PF^* is the reference power factor, which should be above 0.92. Fig. 3 shows a fixed capacitor bank for a given voltage and kvar rating.

Figure 3 – Capacitor bank with fixed kvar rating. (WGR Ignitron, 2020)

These fixed banks are interesting for a fixed load, with a well known pattern, such as transformers operating at no load. Normally, industrial loads tend to oscillate over a mean value for active and reactive power. This means that a fixed capacitor bank can correct the mean PF, but it is not effective on correcting it instantaneously. For this reason, the automatic capacitor banks are normally used. Fig. 4 shows an automatic capacitor bank.

These capacitor banks consist of tapped capacitive branches with different rated kvar power. Through an automated system using relays and an automatic PF controller, this

Figure 4 – Automatic tapped capacitor bank. (JHMppe, 2020)

system can measure instantaneous active, reactive and apparent power and continuously correct the PF. This bank is designed through the rated voltage line and maximum Q_C needed.

Also, these automatic capacitor banks demand automation and the construction of a complex panel, composed by the capacitors, contactors to execute the maneuvers and PF automatic controllers which implement the logical operation. As an example, an automatic capacitor bank of 10 kvar is currently in a range of $ 1500.00, changing this price for each manufacturer.

2.2 PV Inverter Modeling and Control Strategy

The conversion to the ac output is made accordingly to Fig. 5. The inverter is driven in order to generate three 120° phase-shifted sinusoidal signals, however the output voltage is a PWM with amplitude $-v_{dc}$ e $+v_{dc}$. It is necessary a filtering process to obtain the output waveform with the desired frequency.

Commonly, the filters used in the commercial inverters might be a second order LC or a third order LCL filter. The LC filter presents great attenuation for high frequency, however this topology presents high inrush currents in the output capacitance, with possibility of resonance with the grid. On the other hand, the LCL filter have greater attenuation of -60 dB/dec when compared to the -40 dB/dec of the LC filter by adding a second inductance, which limits the inrush current in the capacitor. However, its complexity and volume is increased due to the other inductor. Both filters also have an resonance frequency, which can amplify harmonic currents (Gomes; Cupertino; Pereira, 2018).

The inverter is chosen through its rated power and voltage levels. However, for simulation purposes, the LCL filter must be specified based on the rated power and

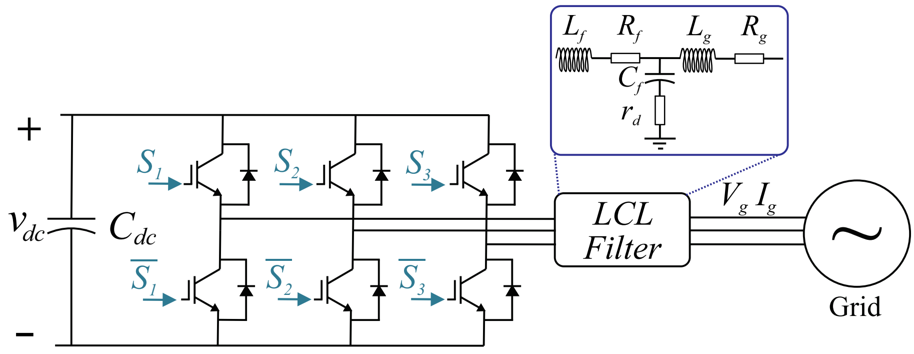

Figure 5 – Grid-connected PV inverter.

the semiconductor switches must be defined in order to study the lifetime evaluation of the inverter. The LCL filter project is made according to the methodology proposed in (Peña-Alzola et al., 2014).

Fig. 6 shows the control strategy adopted in this work. This strategy consists of a dq-coordinate control of the grid currents.

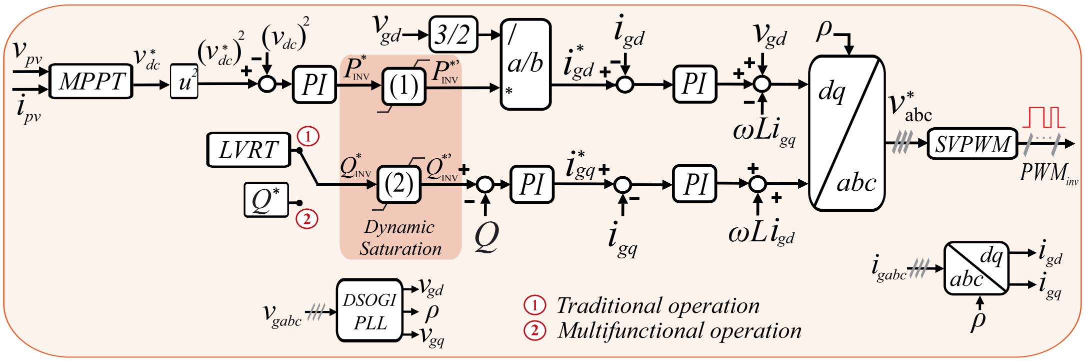

Figure 6 – Control block diagram of a three-phase grid-connected PV inverter.

This control strategy is used for traditional and multifunctional inverter operation modes. The control algorithm is implemented in synchronous reference frame (dq) in two loops (Pereira et al., 2015). The inner loop controls the inverter injected current using traditional PI controllers, what is made possible through Phase-Locked Loop (PLL) structures. The PLL structure allows to synchronize the signals with the phase angle of the grid, what can convert all of the ac signals to dc, enabling linear control.

All of the PI controllers used in the control strategy were implemented with an anti-windup strategy. Since the control used have dynamic saturation, the PI controllers are anti-windup to improve control response in cases of continuous saturation.

The PLL structure used is based on the Dual Second Order Generalized Integrator (DSOGI) PLL, developed in (Rodríguez et al., 2006) and described in Fig. 7.

This structure consists of main three stages: in the first one, two SOGI filters are used in order to generate signals in direct and quadrature axis for the previous transformed

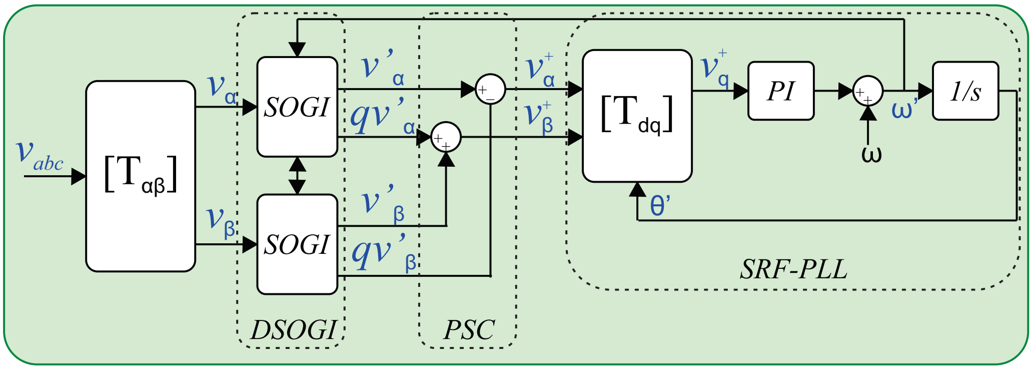

Figure 7 – DSOGI-PLL structure.

alpha-beta signals. This stage also attenuates the incoming signals, mitigating part of the harmonics in the grid voltage.

In the second one, the Positive Sequence Calculator (PSC) takes the direct and quadrature signals and calculates the positive sequence in $\alpha\beta$ coordinates. This result is obtained applying the Fortescue theorem along with $\alpha\beta$ transformation. This stage removes the unbalanced effects of the grid since it extracts only the positive sequence, improving the performance of the further stage.

In the last stage, a common Synchronous Reference Frame (SRF) is applied to the filtered and balanced positive sequence signal. In this stage, the angle of the input signal is correctly extracted allowing to synchronize the control with the grid signals.

The currents are cascaded controlled by using an outer loop for the control of the dc-link voltage and the injected reactive power. In normal conditions, the PV inverter operates with zero reference for the reactive power injection, and supports the grid with reactive power only in the cases of Low-Voltage Ride-Through (LVRT) where it has to support the grid momentarily. Several control strategies addressed in the literature can be implemented (Xavier; Cupertino; Pereira, 2018).

The internal current loop gains are calculated considering that this control is slower than the PWM modulator implemented. This guarantee the system stability in the presence of the computational delay of digital control implementation.

The external loops are calculated in a frequency lower than the one used in the internal loops. In this control strategy, the external loops control the dc-link voltage and the reactive power delivered by the inverter. The dc-link controllers gains are calculated based on the capacitor stored energy and the reactive power is determined through the PQ theory. The gains and their deductions are derived from (Sousa, 2011).

During multifunctional operation, a current dynamic saturation strategy is required to avoid that the inverter operates beyond its rated current. With both reactive and active power reference calculated in the external loops this algorithm can be implemented, as described in Fig. 8. The dynamic saturation strategy is employed to ensure that the converter power capacity is not extrapolated: active power injection is the priority, followed by the reactive power injection if the converter still has a power margin.

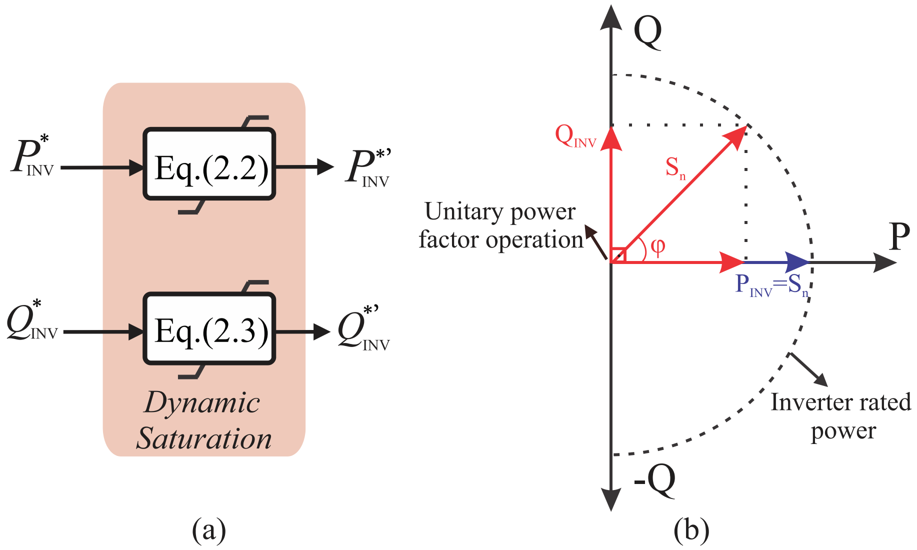

Figure 8 – (a) Dynamic power saturation algorithm. (b) Power calculation scheme based on PQ diagram.

The algorithm saturates the active power reference P^*_{INV} according to (2.2):

$$\left|P^{*'}_{INV}\right| \leq S_n, \tag{2.2}$$

where $P^{*'}_{INV}$ is the saturated active power reference and S_n is the rated apparent power. Subsequently, the new reactive power reference $Q^{*'}_{INV}$ is calculated by:

$$\left|Q^{*'}_{INV}\right| \leq \sqrt{S_n^2 - {P^{*'}_{INV}}^2}. \tag{2.3}$$

Reactive power compensation is total if $\sqrt{{Q^{*'}_{INV}}^2 + {P^{*'}_{INV}}^2} \leq S_n$, otherwise, reactive power compensation is partial. Also, the graphical representation of the PQ values behavior is shown in Fig. 8(b). The vector sum of the PQ values is saturated considering the rated power of the converter, represented by the dashed semicircle. If the active power reference is equal to S_n, then there is no margin to perform reactive power injection. However, if $|P_{inv}| < Sn$, the reactive power reference is calculated, ensuring that the injected apparent power does not exceed the rated apparent power. The dynamic saturation algorithm is computed online and is updated at each control cycle, according to the flowchart shown in Fig. 9.

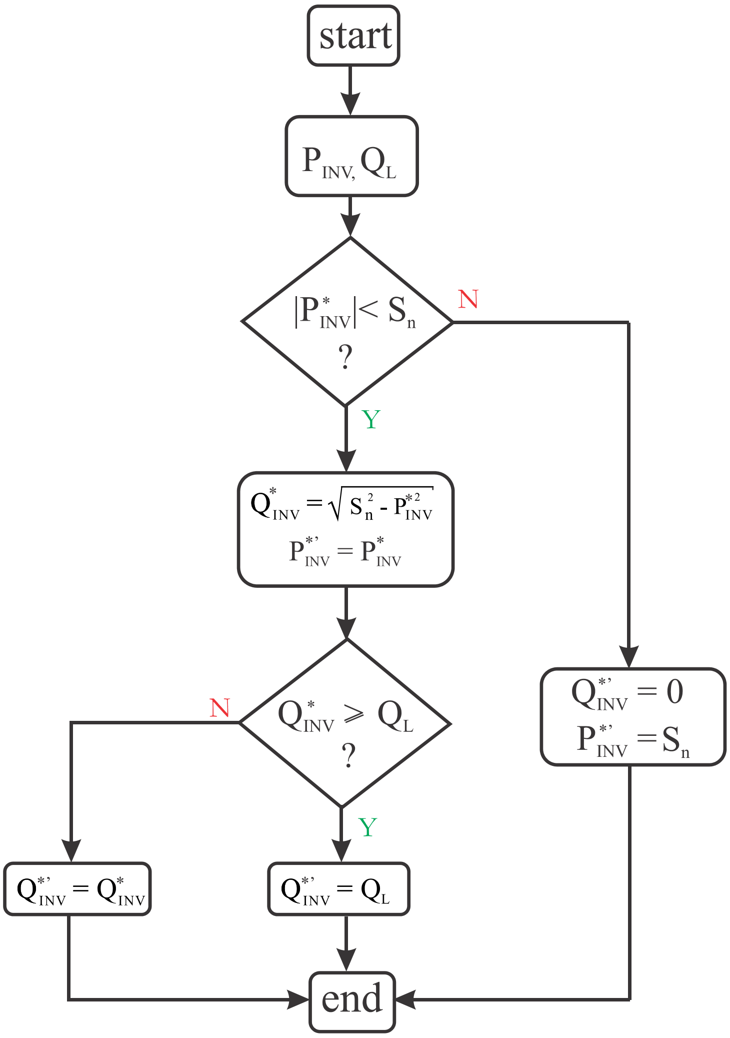

Figure 9 – Flowchart of the dynamic saturation algorithm.

2.3 Theoretical Analysis of PF Reduction with PV Plants Installation

The installation of a PV plant in an industrial environment contributes to drop the PF generating extra fees over exceeding reactive power. Considering P_{INV} as the active power injected by the PV system and P_L the load rated active power, it can be seen that the active power demanded by the grid P_G changes over the day after the PV plant installation, according to:

$$P_G = P_L - P_{INV}. \tag{2.4}$$

A bidirectional energy flow is observed, since the energy demanded from the grid can be positive or negative, depending on the production of the PV plant. A case study is carried out to clarify this behavior. Fig.10 shows the active (P_L) and inductive reactive (Q_L) power profiles requested by an industry on a hypothetical day.

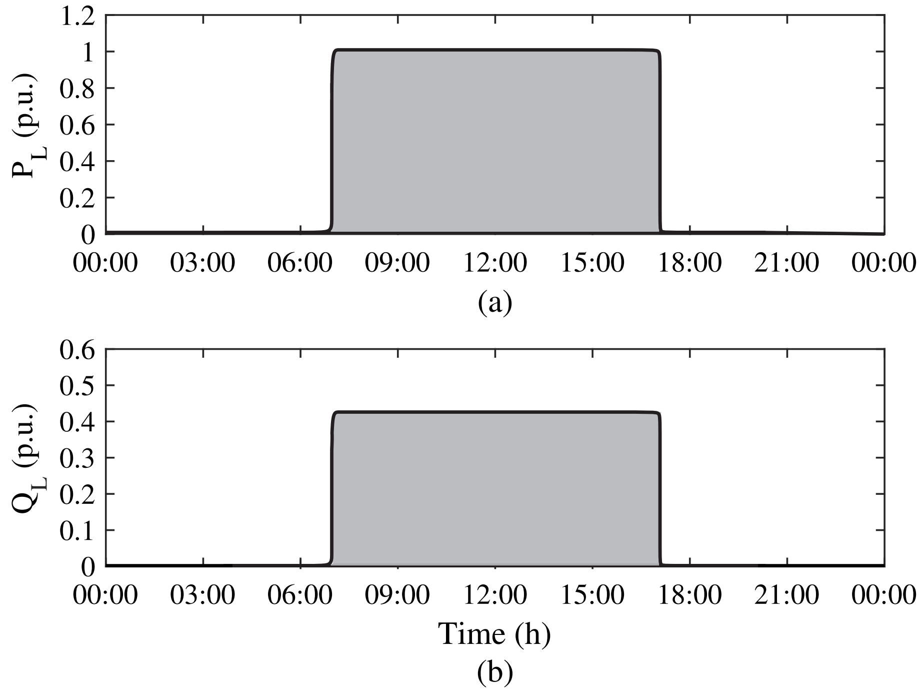

Figure 10 – Rated load powers. (a) Daily active power. (b) Daily reactive inductive power.

Moreover, Fig.11 shows the active power produced by the PV plant on a sunny day, estimated considering the theoretical solar irradiance curves of (Ribeiro et al., 2013). This curve is estimated using the equations of irradiance according to the azimuth and altitude angle from the sun coordinates. This model is very useful to estimate the theoretical irradiance (clean sky approach) at any location and it allows to predict the power generation of PV systems. (Masters, 2004).

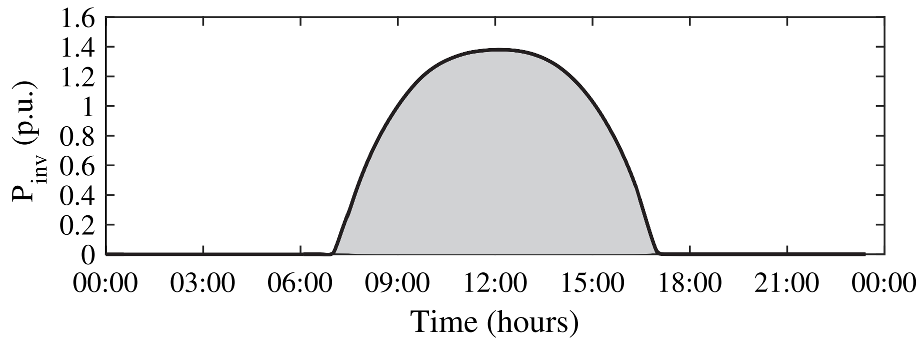

Figure 11 – PV active power delivered by the inverter on a typical sunny day.

Fig. 12 shows the power triangle behavior over time. The active power demanded from the grid is reduced as the PV plant production increases. In such case, the installation PF decreases considerably and can generate charges to the company when it is smaller than the threshold defined by the standards (0.92 was used in this work). It shall be noticed that the triangle to the left is the region where P_G is negative and the triangle to the right represents a positive P_G, being evident the bidirectional power flow. The positive inductive reactive power convention is downward.

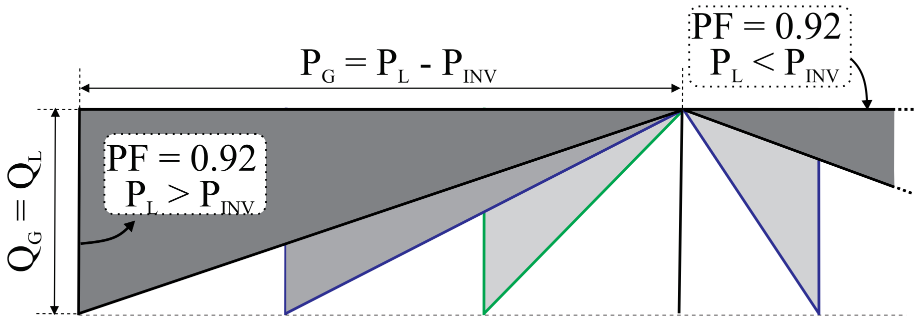

Figure 12 – Effects of the PV plant on the power factor.

An amount of reactive capacitive power (Q_C) is required to regulate the PF within the stipulated range and avoid the PF drop, according to:

$$Q_C = Q_L - |P_G| \tan[\cos^{-1}(PF)]. \tag{2.5}$$

The shape of the necessary capacitive power is shown in Fig.13. The equation to determine this capacitive power uses the absolute value of the grid active power P_G. Even if the power flow can be reversed, the PF must be corrected in either direction since the electric companies use bidirectional meters at the connection point.

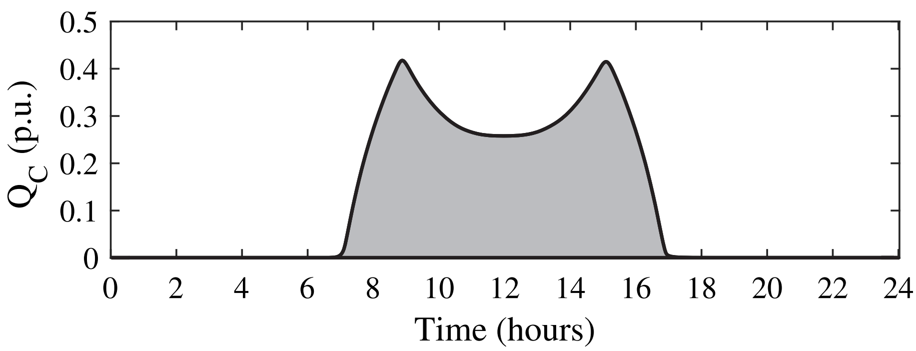

Figure 13 – Demanded reactive capacitive power for correction to 0.92.

Fig. 14 shows the difference in the power factor caused by the PV plant insertion, PF_{PV}, in contrast with the previous power factor of 0.92. The insertion of the changing active power according to irradiance causes harsh drop, even if the reactive power of the industry remains unchanged.

The power factor drops abruptly between 9 a.m and 3 p.m, when there is considerable active power injection by the PV plant. Theoretically, the power factor falls to zero when $P_L = P_{INV}$ (critical points), where the necessary capacitive power must be equal to the load inductive power for correction to unitary power factor.

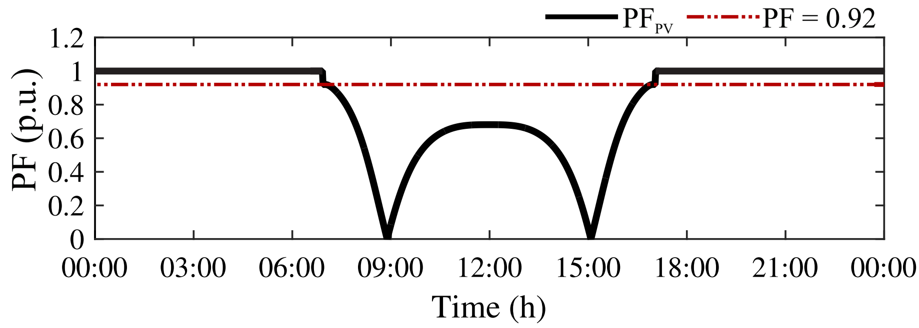

Figure 14 – Change observed in the power factor after the implementation of the PV plant.

2.4 Solutions for dynamic PF correction

2.4.1 Solution based on tapped capacitor banks

A method to correct the PF after PV plant installation is required. Since the profile changes over the day, static solution as fixed capacitor banks are not suitable for this situation. Automatic tapped capacitor banks can do more dynamic profiles by rounding the original curve to fixed steps.

These tapped banks are projected with parallel capacitor branches. By inserting each one, the total capacitive power is changed in a staircase shape. Considering a step size ΔQ_C, the number of taps is:

$$N_{tap} = round\left(\frac{Q_C}{\Delta Q_C}\right), \tag{2.6}$$

and the approximation of the original curve ($Q_{C,T}$) is:

$$Q_{C,T} = N_{tap}\Delta Q_C. \tag{2.7}$$

Fig. 15(a) exemplifies an approximation of the curve, considering a capacitor bank with 5 identical taps. The rounded curve tends to follow the mean value of the original curve, which makes the corrected PF tend to a mean value of 0.92. Instantaneously, on the points that $Q_{C,T}$ is unequal to the original curve Q_C, the power factor will not be corrected to exactly 0.92, instead it will oscillate to values higher and lower than this one. This makes this kind of solution inherent quantization errors due to physical step limitations.

Also, instead of using fixed steps, the tapped capacitor bank can be divided in steps with different values to achieve better performance. For example, if it has 5 taps of: 1, 2, 3, 4 and 5 kvar, the total capacitive power combination can go from 1 to 15 kvar, in steps of 1 kvar. It is equivalent to a fixed step bank with 15 taps. The correction generates some errors in the PF correction due to the quantization error, as seen in Fig. 15(b).

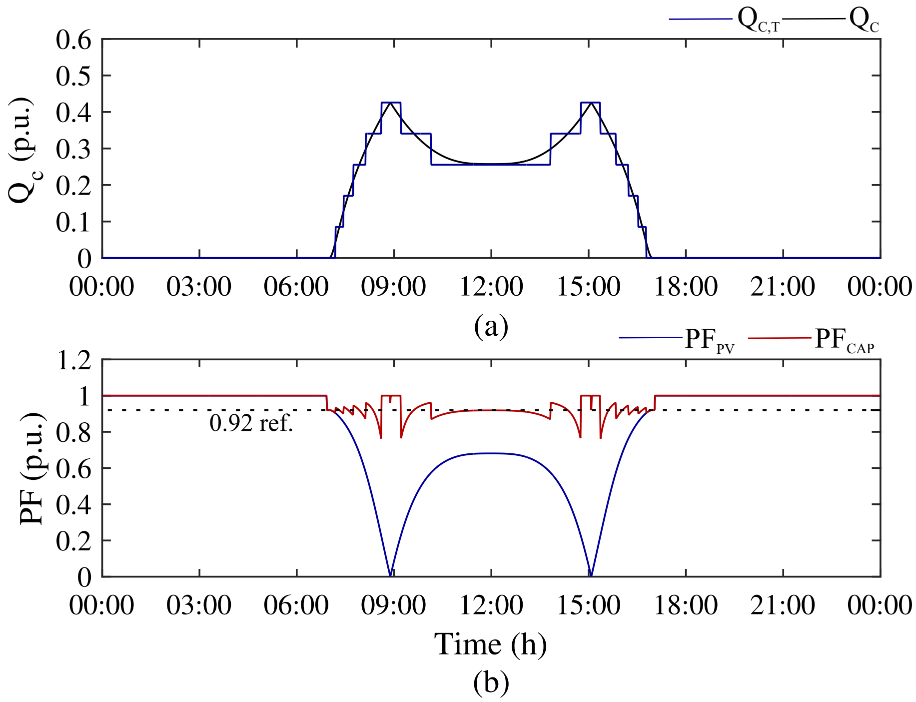

Figure 15 – Correction with tapped capacitor bank. (a) Approximated capacitive power. (b) Corrected power factor.

2.4.2 Solution based on the multifunctional PV inverter

Correction can also be performed by means of multifunctional PV inverters. The PV inverter can inject inductive or capacitive power limited by its rated apparent power S_n. The reactive power which can be injected by the inverter is given by:

$$|Q_{INV}| \leq \sqrt{(kS_n)^2 - P_{INV}^2}, \tag{2.8}$$

where k is the oversizing value, initially set to 1. If the available power is greater than the demanded curve, the inverter can inject the exact amount demanded. Otherwise, the inverter injects reactive power according to its power margin, which results in partial compensation. Thus, $k > 1$ must be employed when the inverter reactive is not able to compensate the total capacitive power.

Fig.16(a) and (b) show the available power of the inverter and the corrected power factor for different values of k, respectively. Due to favorable weather conditions around 12 a.m, the inverter has no power margin to inject the reactive power required by the load for $k = 1$. Inverter oversizing is applied under these conditions in order to allow total PF compensation, as long as the inverter available power exceeds Q_C.

However, additional costs of the multifunctional inverter must be considered due to the use of higher current capacity components. The lifetime of the inverter is directly affected by the amount of processed power, since this increase the operating temperature

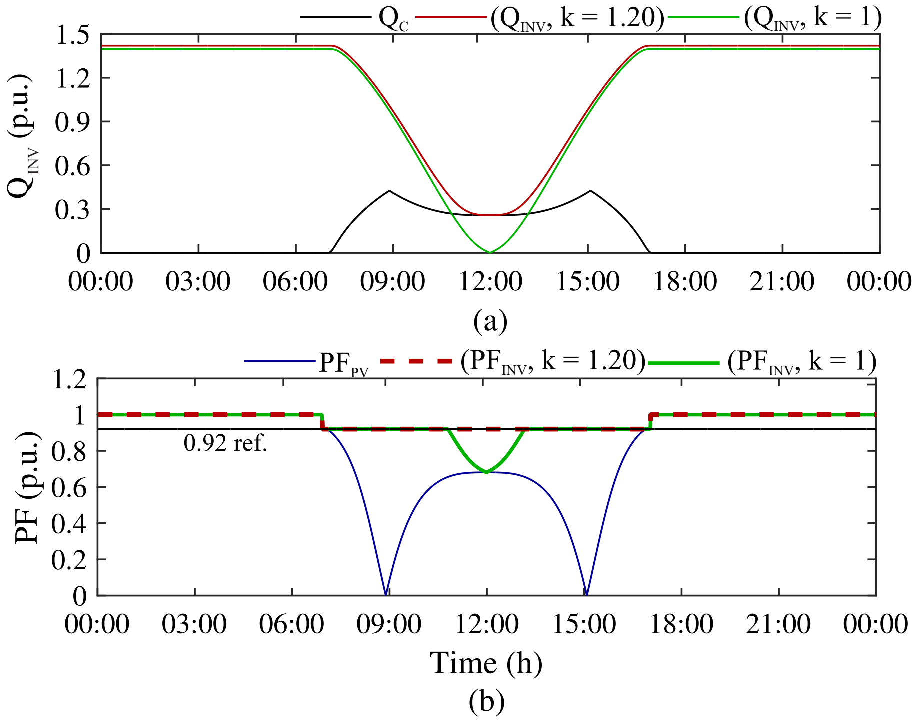

Figure 16 – Correction using the multifunctional inverter. (a) Demanded and available power of the inverter. (b) Corrected power factor.

for every component of the PV inverter, decreasing the total lifetime of the inverter.

By means of oversizing, the PV inverter is able to process more power needed by maintaining lower drop on the total lifetime. In fact, one of the proposals of this work is to determine a value of the constant k in the PV inverter design used to achieve the same lifetime as if it was not processing extra reactive power.

2.5 Chapter Conclusions

In this chapter, the link between the grid connected PV systems and industrial loads were presented. The control strategy is based on modifications in the traditional operation of the PV inverters, considering the dynamic saturation of the power ratings. Also, it is shown how the active power production by the PV plant affects directly the PF, causing harsh drops and generating unexpected fees to the industry.

This PF drop must be corrected in order to reduce these fees, which can be done either by capacitor banks or the multifunctional operation of the inverter. The tapped capacitor banks can achieve good results by using different taps achieving the total needed kvar, but this solution presents rippled correction due to quantization errors. The multifunctional PV inverter can make an accurate correction, however it has limitations in the power injection, since its main focus is in the active power injection into the grid. For the latter solution, an oversizing factor must be included and this parameter is proposed to be obtained by lifetime evaluation.

In the next chapter, the main aspects of reliability theory for capacitor and semiconductors is presented. Also, the methodology used in this work is presented with its characteristics and the lifetime models description.

3 PV Inverter Lifetime Evaluation

In this chapter, the Physics of Failure in semiconductors and capacitors are presented, along with the lifetime methodology implemented in this work. The thermal loading analysis is described on how to change an one-year mission profile into losses in the components and junction or hotspot temperature; the empirical lifetime models are shown, considering their main parameters; at last, the statistical Monte Carlo simulation is described.

3.1 Physics of Failure of Semiconductors and Capacitors

When processing active and reactive power, more current pass through the inverter components, generating extra heating and higher temperatures. Fig. 17 shows thermal images of a commercial PV inverter operating with different power levels. In Fig. 17(a) and (c) the inverter is injecting 600 W of active power. With this condition, the maximum temperature in the two images is 50 °C and 37 °C. In Fig. 17(b) and (d), the inverter is injecting 600 W of active power and 600 var of inductive reactive power. In this situation, the maximum temperature increases to 56 °C and 40 °C, due to the higher currents processed. These higher temperatures decrease the total lifetime of the inverter, which makes this analysis important to this application.

Among the several components present in a PV inverter, the capacitor and power devices are the most fragile components, as can be seen in Fig. 18. Considering both capacitor and power devices, they sum more than 50 % of the occurring failures in the inverter.

The lifetime evaluation of a power converter consists into analyze the behavior of its components in the normal operation. Each component reduces its useful lifetime due to the temperature variations caused by the operation of the converter. The most fragile components in the PV inverter are the semiconductor switches and dc-link capacitors (Reigosa et al., 2016). This leads to the importance of knowing the physics of failure (PoF) for these components.

3.1.1 PoF for Semiconductor Switches

Fig. 19 shows the internal structure of an IGBT module. The main causes of the wear-out failures that occur in this module due to thermal cycling are (Wolfgang, 2007):

- The baseplates joint cracking;

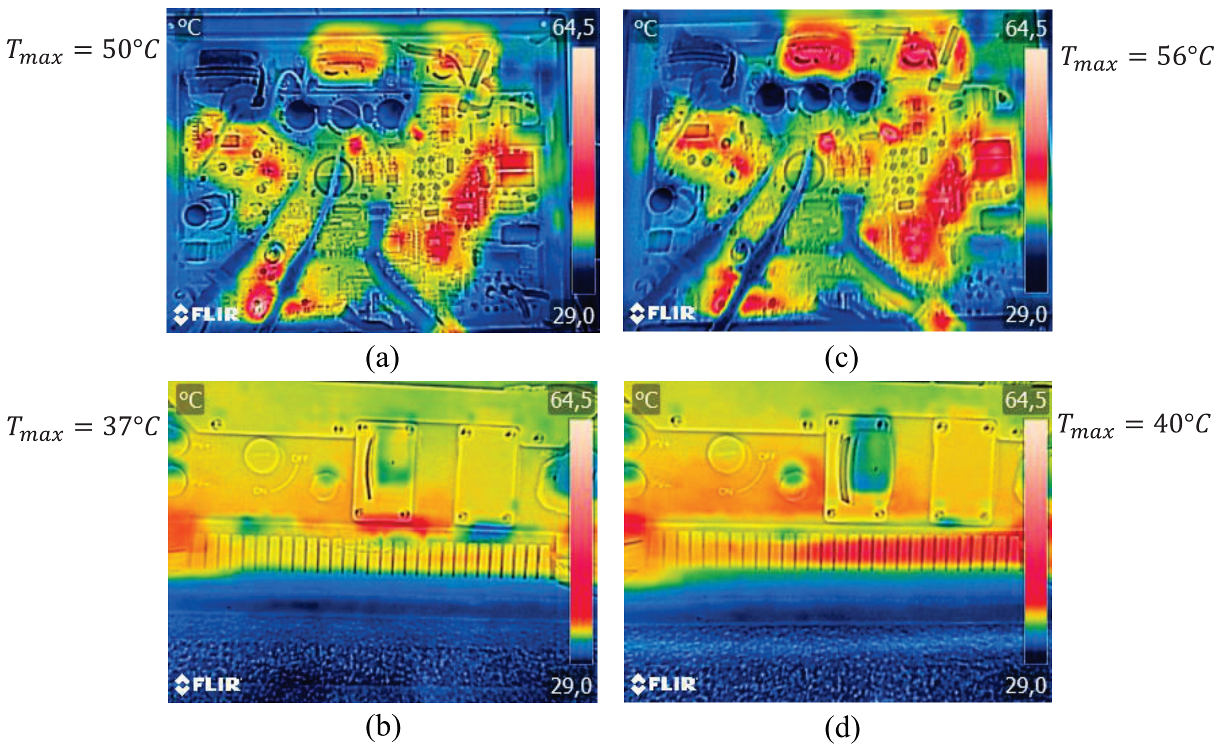

Figure 17 – Thermal images of a commercial PV inverter under different power injections. (a) Active power injection of 600 W, superior view, (b) lateral view. (c) Active and reactive power injection of 600 W + 600 var, superior view, (d) lateral view.

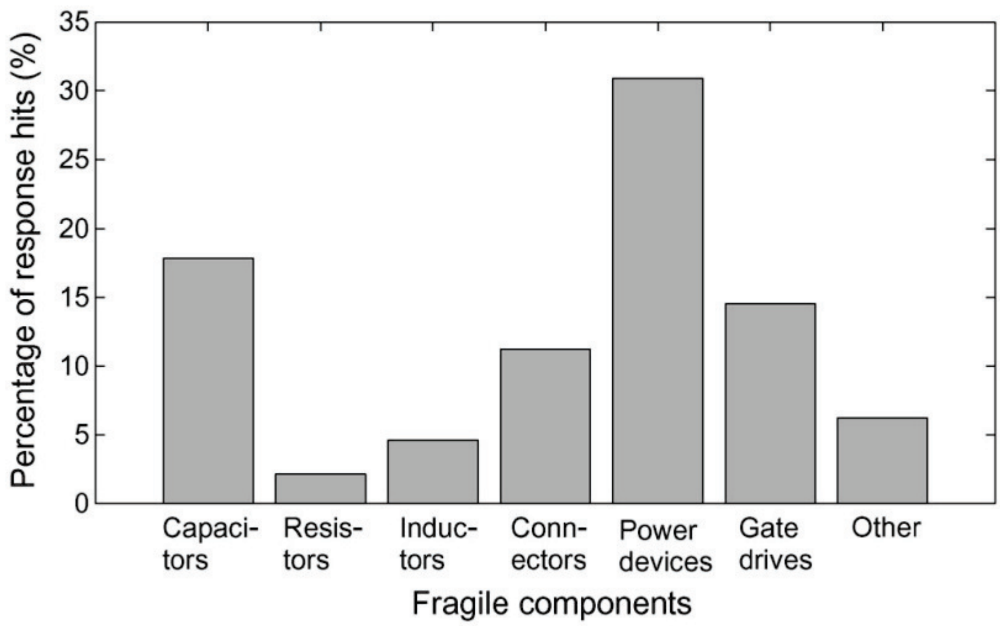

Figure 18 – Percentage of failures in the several components in a PV inverter (Yang et al., 2011).

- Chip solder joint cracking;
- The bond-wires liftoff.

Since the converters operate injecting alternating current based on switching of power devices, there are temperature changes in the module within each cycle of the grid signals. The module is compound of different materials with different thermal constants and this continuously physically bends the inner parts of the module structure, as shown in Fig. 19 (Wolfgang, 2007).

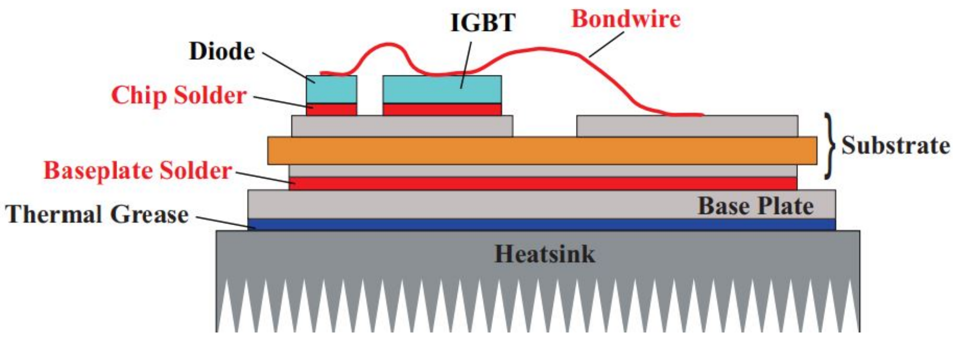

Figure 19 – Structure of an IGBT module (Cupertino, 2019).

Normally the materials in the module operate in an elastic behavior, where they bend, restoring to the original characteristic at each thermal cycle (McPherson, 2010). After many cycles, the materials tend to deteriorate and eventually have a plastic behavior when there is an irreversible deformation causing the module to fail, as shown in Fig. 20. These are known as wear-out failures because they take time to occur and are more predictable.

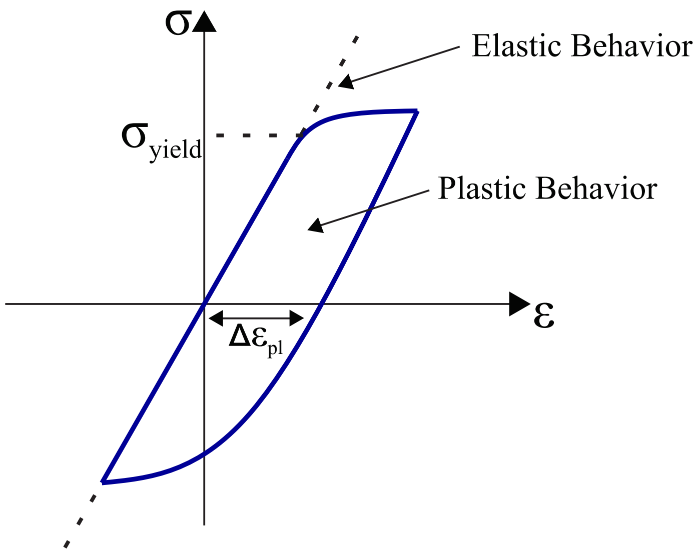

Figure 20 – Stress-strain curve for a material.

Also, there are conditions known as catastrophic failures, caused by imprevisible and highly damaging events, such as short circuit or high-voltage breakdown. These events lead to immediate failure of the module and are very difficult to predict. For these reasons, only the wear-out failure is considered in the lifetime analysis (Wang et al., 2014).

3.1.2 PoF for Capacitors

The dc-link capacitors operate draining energy from the PV arrays, delivering energy to the inverter and, therefore, to the grid. This continuous charge and discharge also wears-off the capacitor in some time of utilization. Also, the constant electrolyte vaporization and electrochemical reactions inside the capacitor contributes to reduce its capacitance and lifetime (Wang et al., 2014). The main capacitors used in the dc-link are:

- aluminum electrolytic capacitors;
- metalized polypropylene film capacitors;
- high capacitance multilayer ceramic capacitors.

Among these three, the aluminum electrolytic capacitors (Al-Caps) are the most used in the commercial inverters. For this reason it is the capacitor focused on this lifetime analysis. Each capacitor has particular parameters to monitor its lifetime consumption and determine when it is completely damaged.

The electrolytic capacitors are compared based on the capacitance value (C) itself and the equivalent series resistance (ESR), which is inherent to the capacitor and usually changes with the frequency. These capacitors are considered in the end of their lifetime when C drops to 80 % of the original value or when ESR increases to 200 % of the original values.

3.2 Thermal loading analysis

When processing reactive power, the multifunctional inverter is subject to higher current and, consequently, higher temperature levels in its components. References (Vernica; Wang; Blaabjerg, 2018) and (Andresen et al., 2018) show that the thermal stress is the main cause of aging failure in the inverter components. Besides, according to (Reigosa, 2014), the inverter critical components are the power semiconductors and dc-link capacitors. In both components, power losses are the main causes of temperature rise due to the thermal impedance of each component layer.

Fig.21 shows the methodology to evaluate the reliability of power modules and capacitors, which consists of three steps: thermal loading analysis, lifetime evaluation and Monte Carlo simulation. A one-year mission profile (MP) of solar irradiance (G) and ambient temperature (T_a) is used to evaluate the converter reliability. The active power produced by the PV array is calculated using the model from (Villalva; Gazoli; Filho, 2009).

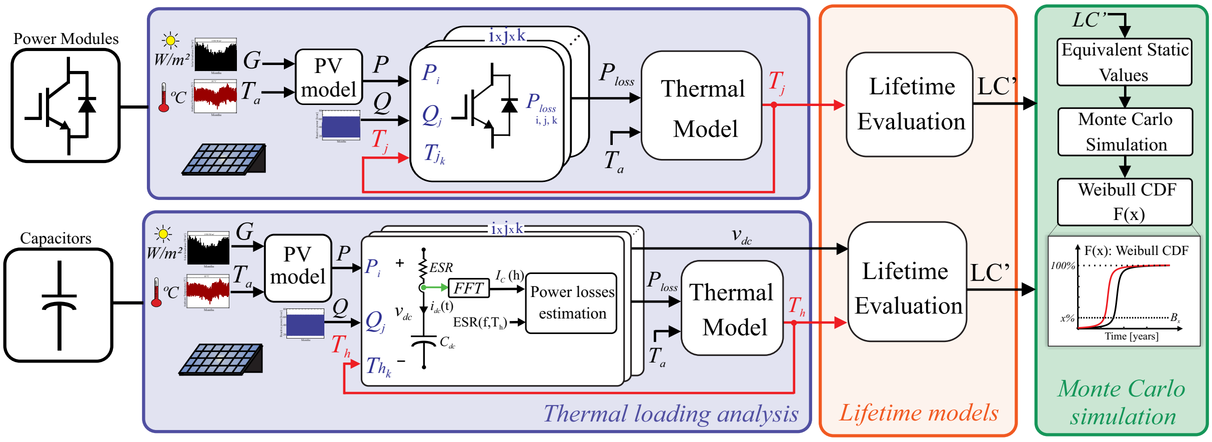

Figure 21 – Flowchart for the lifetime evaluation of power devices and dc-link capacitors.

During reactive power compensation, the inverter operates under higher thermal stress conditions, due to higher current operation. Therefore, the mission profile (based on solar irradiance profiles, ambient temperature and reactive power demanded by the industry) has a strong effect on the PV system reliability. The mission profile must be translated into a thermal loading to obtain the junction temperature (Tj) of the power module and hot-spot temperature of the capacitors.

The block called thermal loading analysis of Fig. 21 shows the main steps to translate the profile into thermal loading. The active power P is obtained from the PV system model considering the mission profile as input. The calculation of the total power losses is implemented with a look-up table, obtained from a certain set of operating conditions: reactive and active power injection as well as fixed junction temperature. This procedure is performed at PLECS simulation environment. The look-up table of the capacitor power losses is developed according to (Wang et al., 2019).

Therefore, the power losses under other conditions given by the mission profile can be interpolated from the look-up table. Once the look-up tables are constructed, the power losses of the devices are estimated. Then, the thermal loading of the semiconductors is determined by means of the equivalent circuit, shown in Fig. 22. All the semiconductors are coupled at the same heatsink, sharing the same thermal network. Therefore, they have the same heatsink temperature. This thermal coupling directly influences the junction temperature of the devices. Also, the Hybrid model is used in this work since the extra Cauer Model grants better prediction of the case temperature (Ma, 2015).

The junction temperature dynamics is affected by (i) weather variations (thermal long-cycles); and (ii) grid frequency (thermal short-cycles). In order to detect the thermal long-cycles, the Rainflow counting algorithm is used to find the heating time (t_{on}), junction temperature fluctuation (ΔT_j) and average junction temperature (T_{jm}). These three parameters are determined according to reference (Ma; Blaabjerg, 2012) for the thermal

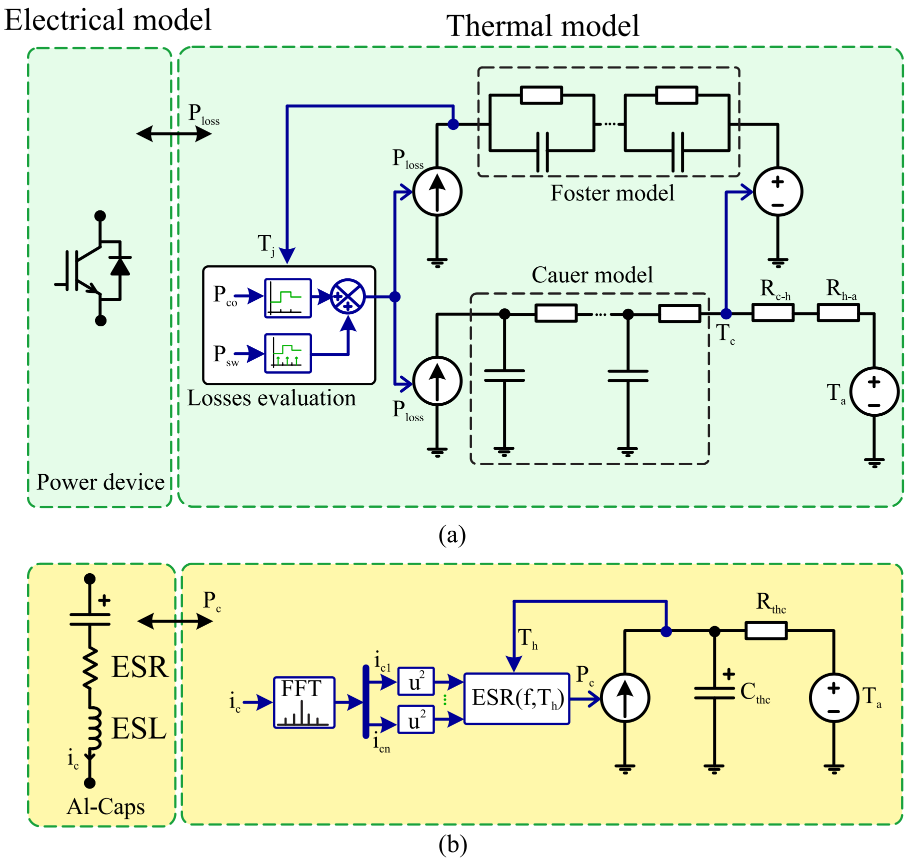

Figure 22 – (a) Hybrid thermal model implemented to determine the T_j for the semiconductors. (b) Thermal model for the Al-Capacitor.

short-cycles.

On the other hand, the dc-link capacitors hot-spot temperature T_h are estimated by the thermal model used in (Cupertino et al., 2019). The capacitor ohmic losses are computed by considering the sum of the contributions of the capacitor current spectrum, from 60 to 100 kHz. Then, the capacitor hot-spot temperature is obtained using a thermal model by means of:

$$T_h = T_a + R_c \sum_h ESR(hf_n, T_h) I_c^2(hf_n), \tag{3.1}$$

where R_c is the equivalent thermal resistance from hot-spot to ambient, h is the harmonic order, $ESR(hf_n, T_h)$ is the equivalent series resistance at frequency hf_n and at hot-spot temperature T_h and, finally, $I_c(hf_n)$ is the RMS value of the ripple current at frequency hf_n.

3.3 Lifetime models

The lifetime models for semiconductors and capacitors are given in (3.2) and (3.3), respectively (Scheuermann; Schmidt; Newman, 2014).

$$N_f = A\Delta T_j{}^{\alpha} ar^{\beta_1 \Delta T_j + \beta_0} \frac{C + t_{on}{}^{\gamma}}{C+1} e^{\frac{E_a}{k_b T_{jm}}} f_d \tag{3.2}$$

$$L = L_0 \left(\frac{v_{dc}}{V_0} \right)^{-n} 2^{\frac{T_0 - T_h}{10}}, \tag{3.3}$$

where N_f is the number of cycles to failure for each MP stress condition. f_d is defined as 1 for IGBT and 0.6204 for diode. L and L_0 are the lifetime under operating and testing conditions, respectively. v_{dc} is the operating dc-link voltage and V_0 is the voltage at test condition. T_0 is the temperature under test condition. n refers to the voltage stress exponent, defined between 1 and 5. The other parameters are defined in (Scheuermann; Schmidt; Newman, 2014).

Equation 3.2 is known as Scheuermann Model and this lifetime model includes the cycle heating time t_{on} effect together with the effect of other bond wire parameters. Eq. 3.3 includes the total voltage of the bus, showing that higher voltage at the dc-link decreases the lifetime of the capacitor.

Moreover, it is assumed that the damage contribution in both components due to each thermal cycle is accumulated by means of the Miner's rule (Sangwongwanich et al., 2018b), according to (3.4) for the semiconductors and (3.5) for the capacitors.

$$LC' = \sum_k \overbrace{\frac{1}{N_{f(l)_k}}}^{long-cycles} + \overbrace{\frac{f_n T_s}{N_{f(s)_k}}}^{short-cycles} \tag{3.4}$$

$$LC' = \sum_k \frac{T_s}{L_k}, \tag{3.5}$$

where f_n is the grid fundamental frequency; T_s is the MP sampling time; $N_{f(l)}$ and $N_{f(s)}$ is the number of cycles to failure due to the contribution of thermal long and short-cycles, respectively, and L_k is the time-to-failure for each MP sample.

3.4 Monte Carlo simulation

The lifetime consumption (LC') obtained through the Miner's rule suggests that the components degrade equally and fail at the same time, which is not observed in field experiments. In order to consider the tolerances of the manufacturing process and the different levels of thermal stress experienced by the components, a Monte Carlo statistical simulation is applied as seen in Fig. 23, based on (Reigosa et al., 2016).

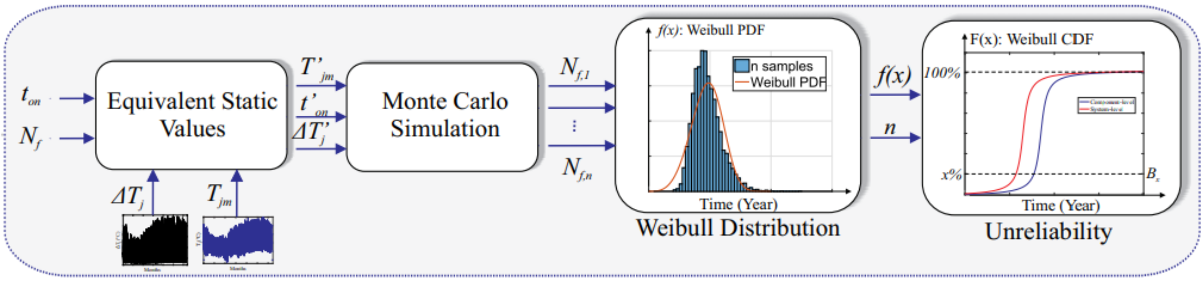

Figure 23 – Monte Carlo statistical evaluation. (Callegari, 2018)

Firstly, it is necessary to find the static equivalent parameters of the lifetime models in order to obtain the same LC'. Subsequently, the Monte Carlo analysis is simulated for N samples and a fit is performed using the Weibull probability density function (PDF) $f(x)$. The cumulative density function (CDF) $F(x)$ represents the component unreliability of the PDF $f(x)$, while the system unreliability is given by:

$$F_{sys}(x) = 1 - [1 - F_i(x)]^{n_i}[1 - F_d(x)]^{n_d}[1 - F_c(x)]^{n_c}, \tag{3.6}$$

where $F_i(x)$, $F_d(x)$ and $F_c(x)$ are the unreliability functions of the n_i IGBTs, n_d diodes and n_c capacitors, respectively. Eq. (3.6) considers that all devices converge to the same cumulative density function.

The survey (Falck et al., 2018) shows an expected lifetime target of 20 years for traditional PV applications. In this work, B_{10} is the reliability metric used to evaluate the system lifetime, which refers to the time when 10 % of the samples have failed (Sangwongwanich et al., 2018a).

3.5 Chapter Conclusions

In this chapter, the Physics of Failure for semiconductor and capacitor were described. Also, the methodology for detecting the lifetime consumption for these two types of components is shown. The total lifetime of these components is directly affected by the thermal cycling, whether it is for physical tension on the semiconductors or electrolyte vaporizing for the capacitor.

The first step of the methodology consists on the thermal loading analysis. It consists of simulating the PV system with a mission profile consisting of irradiance and temperature and obtaining a lookup table with inputs for: irradiance, temperature and junction temperature, with the semiconductor losses as output. For the capacitor, the currents on the capacitor are collected. Then, the junction temperature (T_j) for the semiconductors and the hotspot temperature (T_h) for the capacitors are collected.

These temperatures are fed in the empirical lifetime models to obtain the number of cycles to failure for each element. The damage contribution for both components is them accumulated using Miner's rule considering long and short cycles.

At last, the Monte Carlo simulation is used implementing statistical models based on a Weibull distribution calculating the LC of N different samples. In the end, the unreliability function of the system is obtained. Through this function, the probability of 10 % of the components fail is defined as its useful lifetime in years.

In the next chapter, the case study for this work is presented. The parameters for simulation, mission profiles and figure of merits are described.

4 Case Study

In this chapter, the collected data from real installations is considered in the previous described methodology. The active and reactive power profiles are presented, along with the irradiance and temperature profiles; the PV plant is sized through this data, determining the number of panels and inverters which would be used in this application; the economical parameters used in this work are described, showing the parameters that are evaluated; at last, the thermal parameters that are used in the lifetime evaluation are addressed.

For further analysis, the data from the active and reactive powers were measured at the point of connection of a food industry to the grid, located in the city of Viçosa, MG. These one-week data were measured with a one-second sample time and was extended to complete one year of power profiles, as presented in Fig. 24. As a remarkable improve in this work, a one-year entirely measured PQ profile can be used. Using this approach, the annual variations on the industry production can be addressed as well. The irradiance and temperature data were collected from the online generation data available from the UFG PV plant installation.

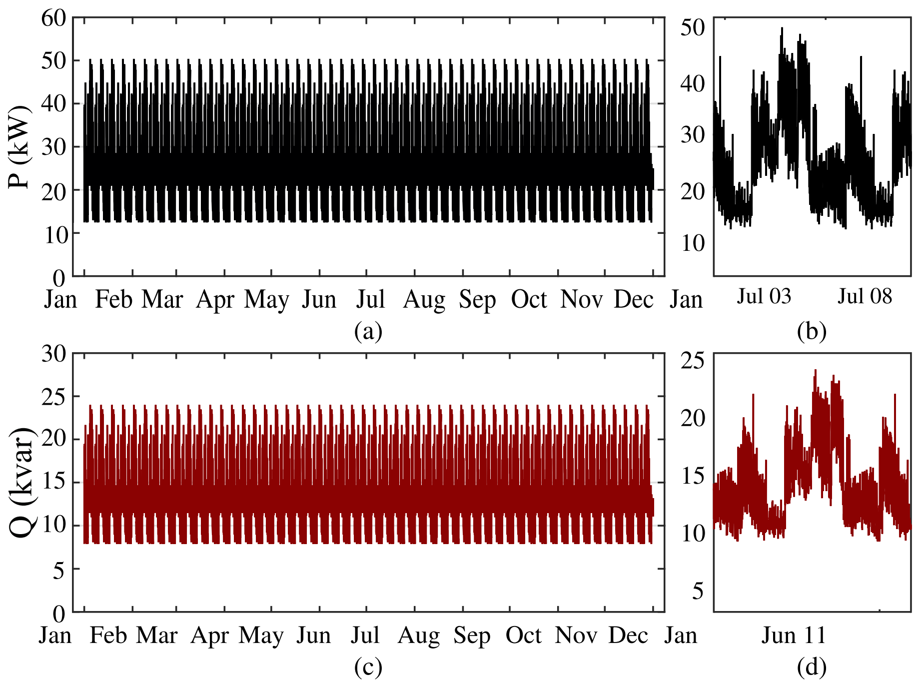

Figure 24 – Active and reactive power data of the industry in 2017. (a) Active power. (b) Zoomed view of July 3. (c) Inductive reactive power. (d) Zoomed view of June 3.

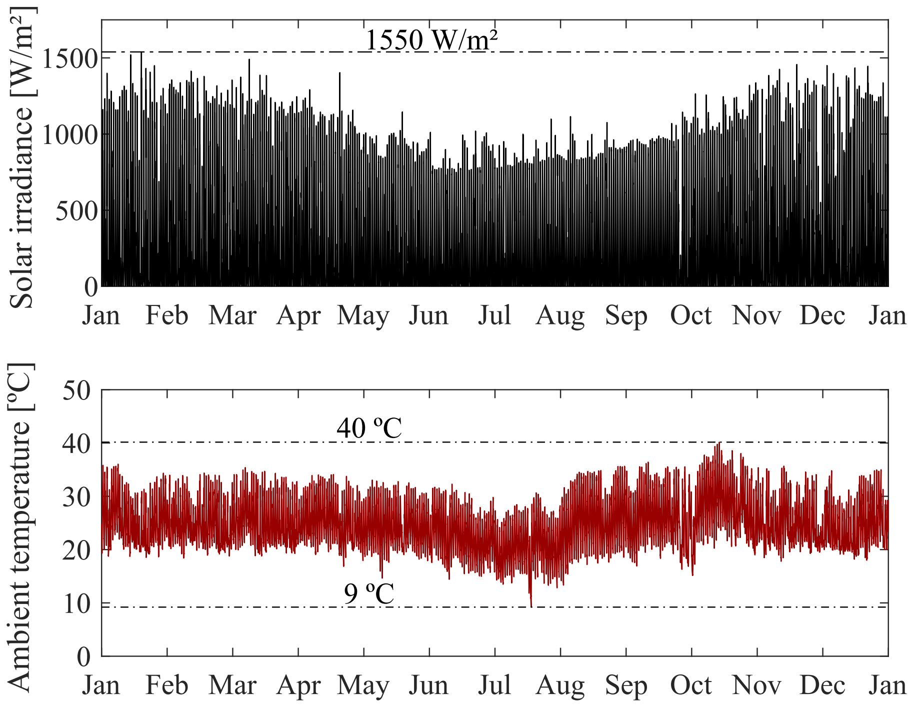

Figure 25 – Mission profile of: (a) Solar irradiance 1-year profile. (b) Ambient temperature 1-year profile.

4.1 PV plant sizing

A PV plant was designed to reduce the electricity bill of this industry, according to the ambient temperature and solar irradiance profiles shown in Fig. 25. The PV plant can be sized using the solar irradiance and active power data. The daily energy generated through a PV panel is given by:

$$E_{panel} = \frac{24\overline{G}A_p\eta}{1000} \quad [\text{kWh/day}], \tag{4.1}$$

where $\overline{G}$ is the average local irradiance in W/m$^2(fromFig.25(a))$,A$_p$ is the area of the panel and η is the efficiency of the panel. The average irradiance in Viçosa is about 4.918 kWh/m^2.day.

Using the profile of active power for the industry, the daily average energy consumed $E_{industry}$, in kWh/day, can be calculated. Using both energies, the number of panels N can be determined by rounding Eq. 4.2 to the next integer.

$$N = \left\lceil \frac{E_{industry}}{E_{panel}} \right\rceil. \tag{4.2}$$

The PV panel used in this work is the 395 Wp from Canadian Solar. Its parameters are shown in Tab. 1.

Table 1 – PV panel characteristics (CanadianSolar, 2018).

Symbol	Parameter	Value
P_{max}	Rated Maximum Power	395 W
V_{mp}	Maximum Power Voltage	38.5 V
I_{mp}	Maximum Power Current	10.26 A
V_{oc}	Open Circuit Voltage	47 V
I_{sc}	Short Circuit Current	10.82 A
η	Module Efficiency	17.88 %
A_p	Area of the Module	2.21 m^2
N_s	Number of Cells	72

With the given data from Tab. 1 above, and using Eq. 4.1, the energy generated by one panel is determined to be:

$$E_{panel} = \left(4.918\frac{\text{kWh}}{\text{m}^2\text{day}}\right)\left(2.21\text{m}^2\right)0,1788 = 1,94\ \frac{\text{kWh}}{\text{day}}. \tag{4.3}$$

The energy demanded from the industry is calculated directly from Fig. 24(a). The mean value of active power is calculated and is given by 23.25 kW. Thus, the energy demanded by the industry is given by:

$$E_{industry} = (23.25\text{kW})\left(24\frac{\text{h}}{\text{day}}\right) = 558\frac{\text{kWh}}{\text{day}}. \tag{4.4}$$

Therefore, the number of panels required is:

$$N = \left\lceil\frac{558}{1.94}\right\rceil = \lceil 287.63\rceil = 288. \tag{4.5}$$

Thus, using the given data, 288 panels of 395 W each are required. With these panels, the total dc power generated by the arrays is 113.75 kWp. The active power generated is converted to ac power by using 4 inverters with rated power of 25 kVA each. The manufacturer's datasheets show that the inverter can work with up to 15 % overload connected on its dc side (phbSolar, 2016), which expand their capacity to over 115 kVA in total. The inverter parameters are shown in Tab. 2.

The PV power delivery by the inverter is determined applying the mission profile to a PV simulator, along with the inverter itself. The active power delivered is shown on Fig. 26.

As seen in Fig. 26, the active power delivered by the PV inverter is subjected to a dynamic saturation on the rated capacity of the 4 inverters, considering the 15 % margin. This occurs as explained in the control strategy. The controller gains are calculated and shown in Tab. 3. These gains were calculated with the equations mentioned in Chapter 2.

Table 2 – Parameters of the three-phase grid-connected PV system.

Parameter	Label	Value
Rated apparent power	S_n	25 kVA
Switching frequency	f_{sw}	16 kHz
LCL filter inductance	L_f, L_g	0.14 mH
LCL filter capacitance	C_f	12.6 μF
LCL filter damping resistor	r_d	1.5 Ω
Grid voltage (RMS)	V_g	380 V
dc-link voltage (v_{dc})	v_{dc}	630 V
Grid fundamental frequency	f_n	60 Hz
dc-link capacitance	C_{dc}	1.7 mF

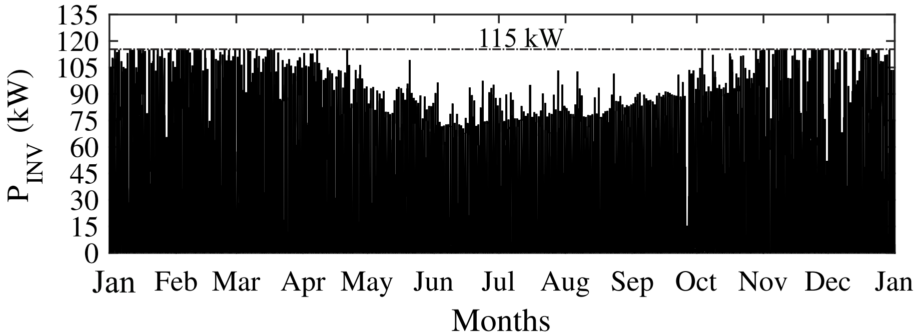

Figure 26 – Active PV power delivered by the inverter.

Table 3 – PI controllers tuning gains.

Parameter	Value
Current proportional gain ($K_{p,cur}$)	1,131
Current integral gain ($K_{i,cur}$)	42,64
Bus control proportional gain ($K_{p,bus}$)	-5,06
Bus control integral gain ($K_{i,bus}$)	-318,17
Reactive control proportional gain ($K_{p,rea}$)	-0,0011
Reactive control integral gain ($K_{i,rea}$)	-0,4284

In the Results Chapter, experimental data is demonstrated as a form of proof of concept, describing how the control of reactive power is made in a PV multifunctional inverter.

4.2 Economical evaluation

On the first term, the fees charged over low power factor are compared using the tapped capacitor bank. In accordance to the Brazilian standard (ANEEL, 2010), the fee due to low power factor is given by Eq. 1.2.

The cost of implementing a multifunctional inverter is defined by the initial investment given for this correction method. Due to the need for oversizing, it is necessary to obtain a new inverter with higher rated power, which means a higher investment cost. The market prices of several different rated inverters were gathered to describe a curve of oversizing factor vs investment. The main focus of describing this curve is to show how much the cost is added by using a higher rated inverter to preserve the lifetime while correcting the power factor.

Also, an inverter with higher rated power has more losses associated, due to more power processing by its components. These losses are calculated based on the lifetime methodology, using the conduction and switching losses for the semiconductors and the total loss of the capacitor. This energy lost is associated with the oversizing factor plotting curves with comparison between power factor correction and loss cost.

4.3 Thermal Parameters

The thermal parameters consist mainly of the thermal resistances within each layer of the components. The lifetime models are empirically determined and its parameters are described by the manufacturer. The foster resistance and thermal constant for the IGBT and Diode are described in the Tab. 4 (Infineon, 2013).

Table 4 – Foster model parameters for the 75 A IGBT Module.

Parameter	1	2	3	4
$R_{thi}(IGBT)$ [K/W]	0.032	0.062	0.312	0.543
$\tau_i(IGBT)$ [s]	0.0005	0.005	0.05	0.2
$R_{thi}(Diode)$ [K/W]	0.059	0.137	0.502	0.602
$\tau_i(IGBT)$ [s]	0.0005	0.005	0.05	0.2

The capacitance on the table above is calculated through the expression of the thermal constant, described by:

$$C_{thi} = \frac{\tau_i}{R_{thi}}. \tag{4.6}$$

Also, the thermal resistances for the case-to-heatsink were derived from the datasheet of both components. Being determined as $R_{c-h} = 0.35$ K/W for the IGBT and Diode. The heatsink was dimensioned to present about $R_{h-a} = 0.5$ K/W due to the high dimension of the inverter. The hotspot-to-ambient resistance is determined through (Cupertino et al., 2019), being $R_c = 2,3$ K/W. Also, the ESR curve through each frequency is extracted from the datasheet of the capacitor, with the rated temperature of 85 °C (EPCOS, 2016).

For the physical semiconductors and capacitors used in this work and for lifetime evaluation were designed for the according application. The considered inverter was designed with 1200 V/75 A power module, with part number FS75R12W2T4 from Infineon as shown in Fig. 27.

Figure 27 – IGBT and Diode power module.

The dc-link capacitor bank was designed with 10 capacitors (B435*2A6687M0) of 680 μF, arranged in 5 branches of 2 capacitors in series (5x2). These capacitor are arranged in order to endure the voltage and current applied to the dc-link. They are shown in Fig. 28.

Figure 28 – Capacitors of the dc-link.

In the results section, the temperature of the components are shown, along with their lifetime distribution. The lifetime is compared with P only and PQ injection, with the latter decreasing the total lifetime of the converter. Also, an oversizing of the IGBT module is done to increase the lifetime with PQ injection to the same level as the P only case. The oversizing is done in two distinct cases: in the first one, the rating of the inverter will be increasing by a k factor to increase its capacity of correction and reducing its operating temperature; in the second one, the 75A/1200V IGBT module is changed to the 100A/1200V module (F3L100R12W2H3). This new module has higher current capacity, heating less for the same operating point. Also, in the second one, one more capacitor branch is added to increase the total respective lifetime of the capacitors. The foster model parameters of the second IGBT module is described in Tab. 5

Table 5 – Foster model parameters for the 100 A IGBT Module.

Parameter	1	2	3	4
$R_{thi}(IGBT)$ [K/W]	0.084	0.195	0.587	0.584
$\tau_i(IGBT)$ [s]	0.0005	0.005	0.05	0.2
$R_{thi}(Diode)$ [K/W]	0.036	0.156	0.324	0.684
$\tau_i(IGBT)$ [s]	0.0005	0.005	0.05	0.2

4.4 Chapter Conclusions

This chapter describes numerically the case study from which the present methodology is applied. Also, it describes how the values of the parameters used in the inverter simulation are described based on present methodologies of the literature and the main necessary parameters used in the thermal simulation. For the latter, most of them come directly from the manufacturer's datasheet being experimental and empirical data.

The figures of merit are the power factor corrected by the capacitor bank and the inverter, the total fee without and with correction, the price of the inverter according to the oversizing factor implemented, the cost of the loss in the PV inverter for a range of oversizing factors and lifetime and temperature analysis for active power (P) and active+reactive power (PQ).

The next chapter brings the results to the methodology applied. The results demonstrate graphically and numerically the capacity of power factor correction by the solutions and the effects on cost and lifetime evaluation. An oversizing on the PV inverter is done to achieve same lifetime (expected to be over 20 years) while correcting the power factor.

5 Results

In this chapter, the results of this Master Thesis are shown. The fee is calculated considering tapped capacitor banks for different power factor references; the multifunctional PV inverter cost and losses are described for oversizing factor variations; an experimental setup is made to test and validate the saturation structure and the reactive power injection; at last, the lifetime results are addressed through the analysis of the devices temperature and the total lifetime reduction and increment for different oversizing factors and different modules, respectively.

5.1 Simulated Analysis

5.1.1 Power factor correction: tapped capacitor banks

Fig. 29 shows the industry power factor with the implementation of the PV plant. The y-axis shows the fraction of the total hours in one year (8,760h) distribution for the new power factor PF_{PV} without any correction. It is possible to observe that the PF operates mostly in the range between 0.5 and 1, which are considerably low power factors since they are mostly below 0.92.

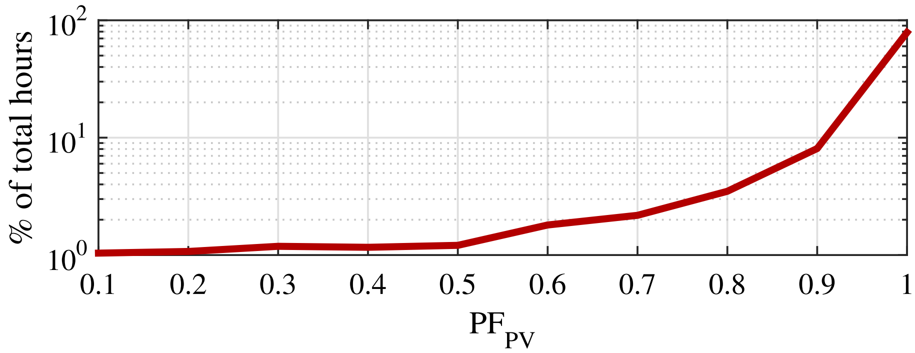

Figure 29 – Power factor after the implementation of the PV system, without power factor compensation strategies.

The maximum value of the demanded capacitive power reaches 21 kvar, which must be achieved with a tapped capacitor bank. The bank received 5 taps. If all of them had the same value, the profile would be approximated in step values multiples of 4.2 kvar, which generates high quantization errors and affects the power factor correction. However, by choosing different taps, more combinations can be achieved. In this work, it is used a capacitor bank with 5 taps of $1, 2, 4, 6$ and 8 kvar. These different taps allow combinations which range from 0 to 21 kvar, at intervals of 1 kvar, resulting in an equivalent bank of

21-tap capacitors. Therefore, a better approximation of the original curve is obtained and, consequently, a better PF correction.

Fig. 30 shows the PF correction result using this 5-tap capacitor bank for different references of PF. Considering a reference of 0.92, this solution does not correct adequately all power factor at the critical points. In order to correct these points, the bank should exhibit the exact value of the original curve, which is difficult to achieve because of the quantization error. The tapped capacitor bank was designed to achieve 0.92 power factor. However, this reference can be changed as well. Fig. 30 shows, also, the number of hours in which the correct power factor is distributed, in a histogram, conducting different references of power factors for the capacitor bank based solution.

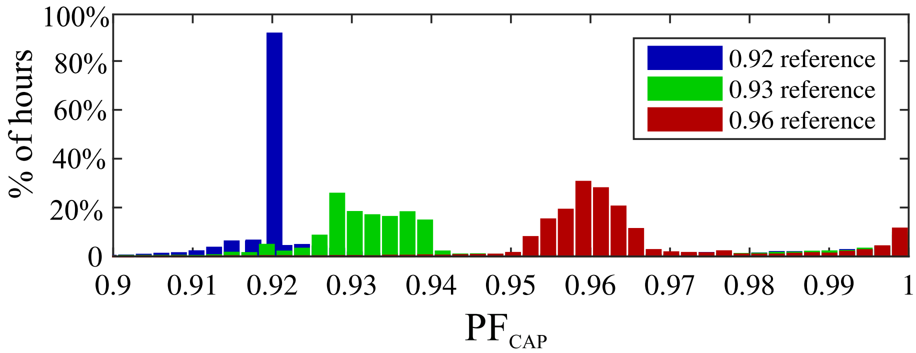

Figure 30 – Distribution for each reference of power factor, using the capacitor bank correction.

The quantization errors caused by the approximation Q_C in discrete steps make the power factor oscillate around the desired reference. By increasing this reference, the corrected power factor gains a margin to oscillate without trespassing the 0.92 limit. Therefore, the correction is more effective as the desired reference increases.

The power factor charges with the capacitor bank correction for 0.92 reference are around \$ 6.00 per year. This value is insignificant, compared to the power factor charge before correction, which was \$ 8,253.00 per year. The charges are almost zero when reference 0.93 is considered, which validates the results shown in Fig. 30. It is considered a base tax of \$ 0.0807 per kWh.

5.1.2 Power factor correction: multifunctional PV inverter

The multifunctional inverter can entirely correct the power factor to 0.92 if its available power surpasses all the necessary reactive power for correction. In fact, the design of the inverter is mainly target at determining the oversizing factor, if needed.

As observed in Fig. 31, the multifunctional PV inverter is described by the number of hours that the corrected power factor remains below 0.92 according to its respective oversize value. For $k = 1$, the inverter cannot compensate the entire demanded capacitive power. If $k >= 1.3$, the inverter can provide full reactive power compensation. However, there is an inherent cost for the use of higher power inverter, since its investment increases as its rated power increases.

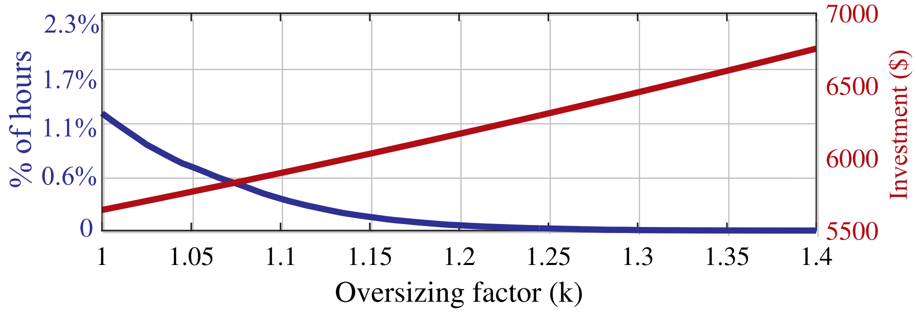

Figure 31 – Investment of the inverter considering the total oversize. The investment curve was made gathering market prices for different rated PV inverters, using a base of 25 kVA for $k = 1$

This is indeed a suitable solution, since the increase in the inverter investment is about \$ 500.00 to make it possible to compensate all of the exceeding reactive power. This value is seen in Fig. 31 when comparing the difference in investment for $k = 1$ and $k = 1.2$. A commercial automatic capacitor bank costs around \$ 1500.00, almost 3 times the extra cost. This increased PV inverter rated power allows it to adequately correct the power factor while occupying less volume than the capacitor bank solution.

Fig. 32(a) shows the total cost of the energy losses in the inverter by increasing the oversizing factor.

These losses were determined through the semiconductors and capacitors in the inverter, considering conduction and switching losses. Higher levels of current generate higher losses and extra costs. The total amount of the PQ injection cost does not exceed \$ 283.00 per year, which is a low value, considering the time range analyzed. Besides, in Fig. 32(b), the power losses due to active power injection only tend to stabilize at the oversize factor in which the PV inverter can inject all active power, i.e, higher values does not affect these total losses.

In summary, the PV multifunctional inverter is an adequate choice for power factor correction. Besides, the higher levels of current in the inverter tend to reduce its lifetime span due to increased losses and temperature. Since the inverter has proved to be a better correction method, a lifetime analysis should be carried out to solve the remaining issues.

5.2 Experimental Proof of Concept

An small scale experimental setup was implemented in order to test the methodology and control proposed and used in this work. The inverter control is programmed in the

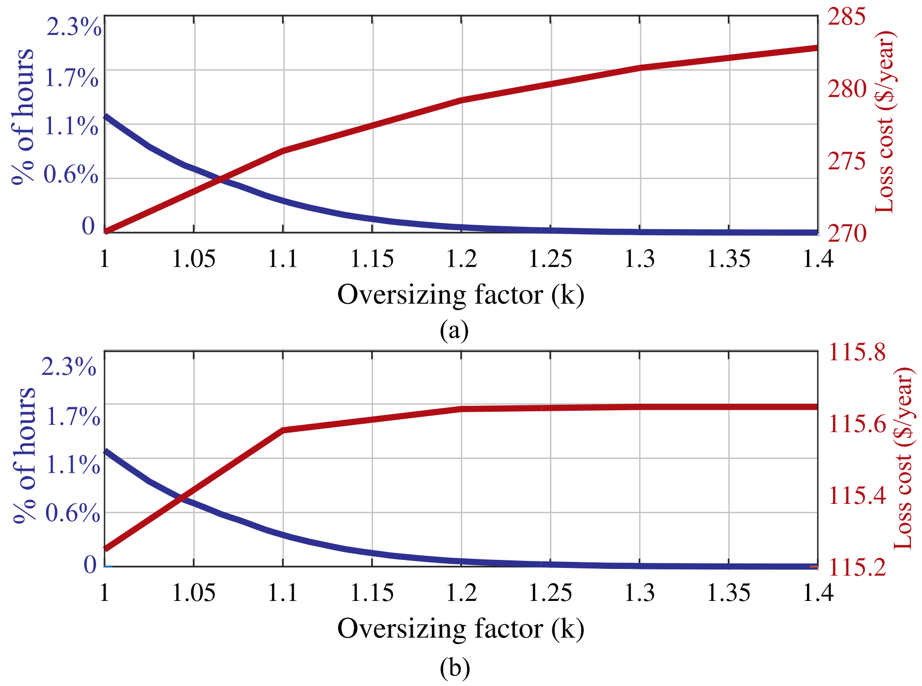

Figure 32 – Cost of the energy losses in the inverter: (a) injecting active and reactive power and (b) injecting only active power. These cost were calculated using a base tax of $ 0.0807 per kWh.

Texas Instruments TMS320F28034 digital signal processor (DSP). The dc-link voltage is supplied by a PV array emulator source, while a grid emulator is connected to converter ac output. The signals are measured using the oscilloscope Tektronix DPO 2014B, with A612 current probe and P5200A differential voltage probes. An overview of the small-scale prototype can be seen in Fig. 33. Moreover, the experimental setup parameters are presented in Tab. 6.

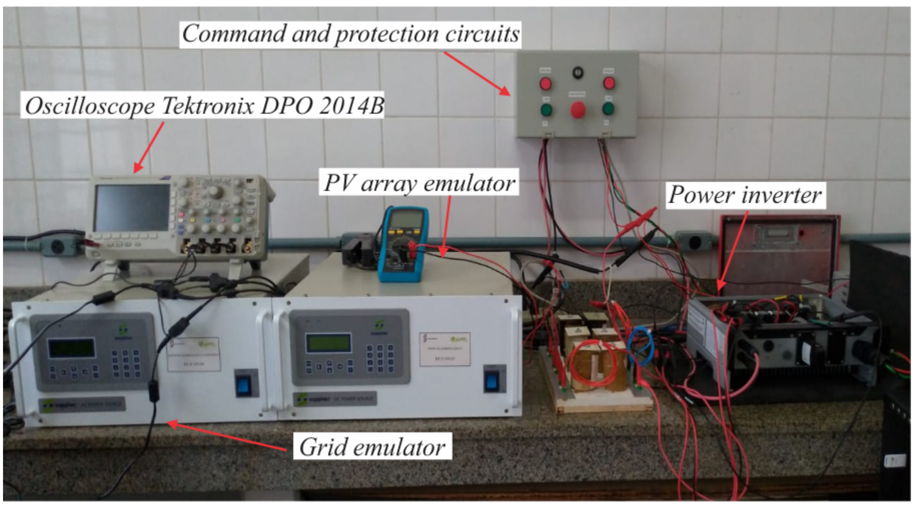

Figure 33 – Experimental setup.

Also, the setup uses a single-phase PV inverter, which demanded small adaptations for the control; they can be seen in (Callegari et al., 2020). Its main focus is to validate the reactive injection using this control in practical aspects. The experimental tests consist of active and reactive power injection variations by the multifunctional inverter to analyze the control dynamic behavior and the applicability of this functionality while the converter has power margin.

Table 6 – Parameters of experimental system.

Parameter	Label	Value
Inverter rated power	S_n	1.5 kVA
PV array rated power	P_{pv}	1.0 kW
Solar irradiance conditions	G	500 W/m^2
Switching frequency	f_{sw}	20 kHz
LCL filter inductance	L_f, L_g	2 mH
LCL filter capacitance	C_f	3.3 μF
Grid voltage (RMS)	V_g	200 V
dc-link capacitance	C_{dc}	1.17 mF
dc-link voltage reference	v_{dc}^*	350 V

Fig. 34 shows the performance of the PV inverter under three different conditions. The traditional operation of the converter is evaluated in the first test, seen in Figs.34(a) and (b). Injected current and grid voltage are in phase as shown in Fig. 34(a).

Under such conditions, the inverter is injecting about 448 W of active power and 20 var of reactive power into the grid. This small amount of reactive power is due to filter impedance, since the current control is made in the inductor before the LC filter. This reactive power is drained by the grid-side capacitor.

Reactive power compensation is enabled in the second experimental test. The inverter is initially injecting active power and a reactive power step is applied, as shown in Fig. 34. No significant transients are observed in the dc-link voltage when the inverter operates in multifunctional mode. The injected current, previously in phase, presents a phase shift φ in relation to the grid voltage, when reactive power injection is performed. Moreover, the current amplitude synthesized by the converter increases by 115 % compared to the conventional operation in such conditions. Regarding the power, about 448 W (unchanged with Q step) and 880.8 var are being processed by the inverter after the reactive power step, resulting in an apparent power of 986 var. These results can be seen in Fig. 34(e).

The last experimental result is shown in Figs.34(c) and (f). The active power processed is 30.68 W (simulating a cloudy day) and the inverter is fully enabled to inject reactive power. In such case, about 880 var are being injected by the inverter and the dc-link voltage is perfectly controlled. Finally, the angle φ is approximately 90°, as expected.

The experimental results showed the PV inverter can flexibly inject reactive power

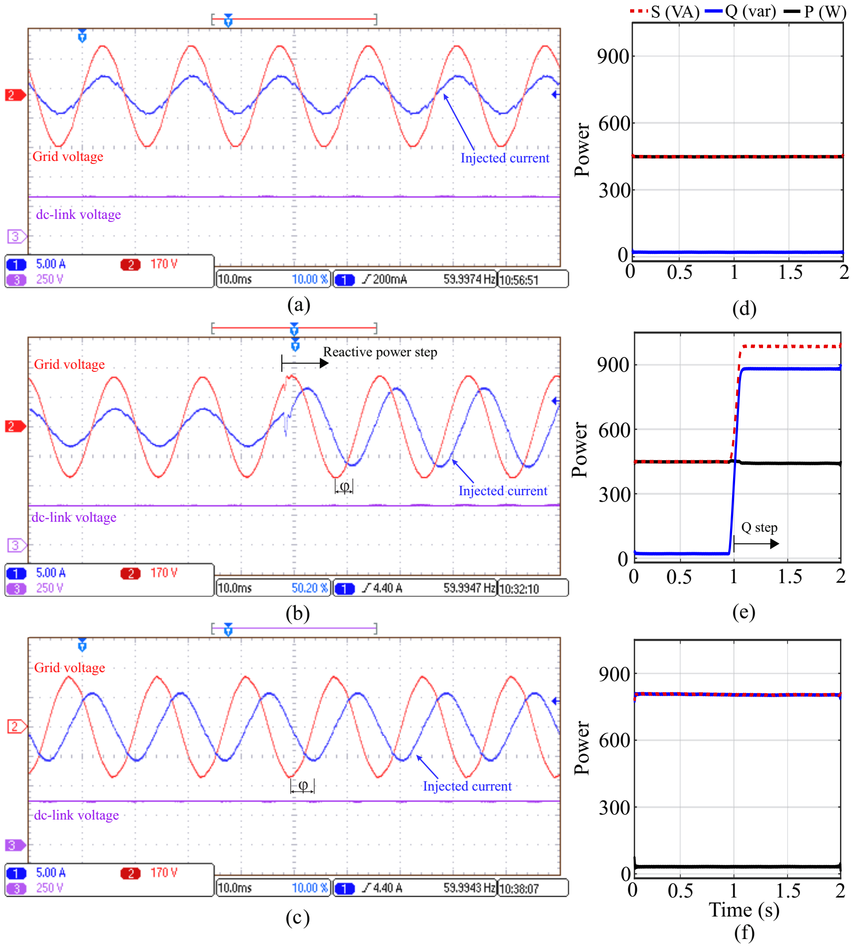

Figure 34 – Experimental results of the setup (grid voltage [170 V/div]; injected current [5 A/div]; dc-link voltage [250 V/div] and time [10 ms/div]). Grid voltage, injected current and dc-link voltage waveforms, considering (a) active power injection only, (b) active and reactive power injection and (c) reactive power injection only. Active, reactive and apparent power injected by the converter, considering (d) active power injection only, (e) active and reactive power injection and (f) reactive power injection only.

to perform PF correction, without harming the dc-link voltage control dynamics. However, the injected current amplitude increases when performing this feature, which may lead to overheating of the inverter components. This is the motivation for the converter reliability evaluation in the following section.

5.3 Lifetime Results

5.3.1 Temperature analysis of the devices

The variation of temperature with the change of power injection is a fine indicator of the lifetime. Fig. 35 shows the temperature in the components of interest to this work: the Diodes, IGBTs and capacitors, without oversizing. The temperatures on the components tend to rise with more power processing, due to higher currents, what decrease their total lifetime. Even a slight increase in the temperature tends to reduce greatly the total lifetime.

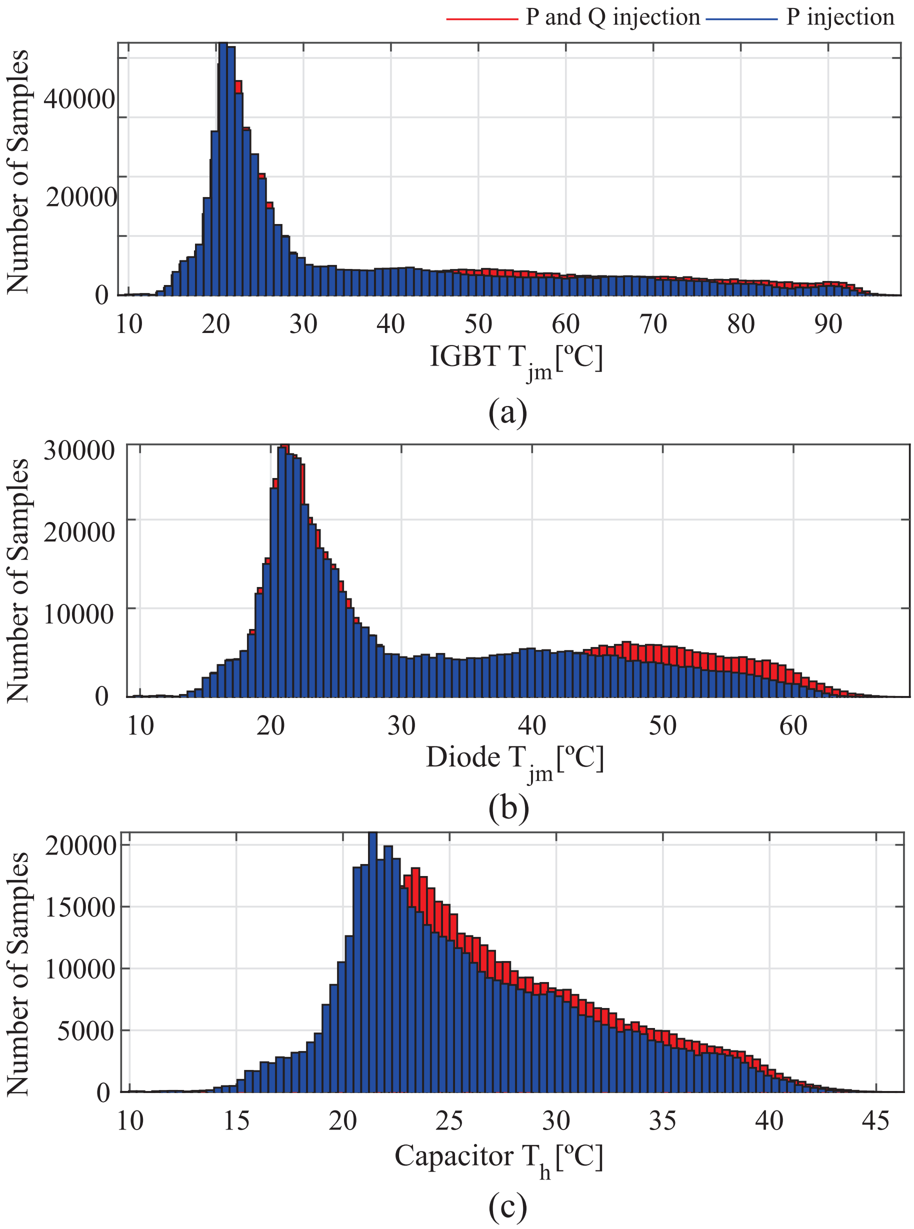

Figure 35 – Junction and hotspot temperatures for only active power (P) injection and active+reactive (PQ) power injection. (a) Diode's junction temperature, (b) IGBT's junction temperature and (c) Capacitor's hotspot temperature.

As can be seen, the variations on the temperature increase slightly, with the greater one being respective to the IGBT junction temperature, for about 15 °C. With the oversizing of the inverter or the IGBT module, these operating temperatures can be decreased, recovering the original lifetime of the inverter.

The hotspot temperature for the capacitors is confined in the range of 20-40 °C as seen in Fig. 35(c). This component have small variation in temperature, what leads to the a great lifetime in general. However, it has also great sensibility on temperature rise as well.

5.3.2 Multifunctional PV inverter reliability evaluation

The inverter is not able to completely inject the reactive power profile requested by the industry if it has no current margin due to dynamic saturation. Thus, two analysis were performed:

- Overload the inverter to inject all the power required, through the oversizing factor k. If $k \geq 1$, the inverter power margin to perform the compensation is greater;
- PV inverter oversizing by increasing the current capacity of the semiconductor devices and dc-link capacitor bank.

Fig. 36 shows the unreliability curves for the first analysis, considering $k = 1, 1.1, 1.3$ and 1.4. The component-level unreliability functions of the semiconductors and dc-link capacitors are shown in Fig. 36(a) and (b), respectively. The impact on system lifetime is not significantly affected by inverter diodes. Therefore, they will not be thoroughly analyzed. Besides, the analyses for $k \geq 1$ consider the injection of active and reactive power.

Regarding the IGBT reliability for $k = 1$ (base case), the B_{10} of the traditional operation is 37 years, while the B_{10} of the multifunctional operation is 27.2 years. A reduction of 26.5 % is observed. Using the same comparison, a 13.33 % reduction is observed for dc-link capacitor (from 33 to 28.6 years).

Fig. 36(c) shows the system-level unreliability function with k variation. There is a reduction of 17.86 % between traditional and multifunctional operation for $k = 1$ (from 22.4 to 18.4 years). By increasing k, a lifetime reduction of both components and system is observed, since the inverter has a higher upper limit of power injection. For 10 % overload ($k = 1.1$), 7.61 % reduction of system lifetime is observed, compared to the multifunctional inverter rated operation ($k = 1$). When this range is increased ($1.1 \leq k \leq 1.4$), the system lifetime is not changed, since the inverter is able to inject almost the entire required power profile at 10 % overload. These results show that the total reactive power compensation requires the overloading of the converter, which reduces the system B_{10} by 24.1 %, compared to the traditional operation for $k = 1$ (from 22.4 to 17 years).

The second study proposed in this section aims to oversize the inverter components to avoid strongly affecting the system reliability due to reactive power compensation. The 75 A/1200 V power module (part number FS75R12W2T4) was replaced by the 100 A/

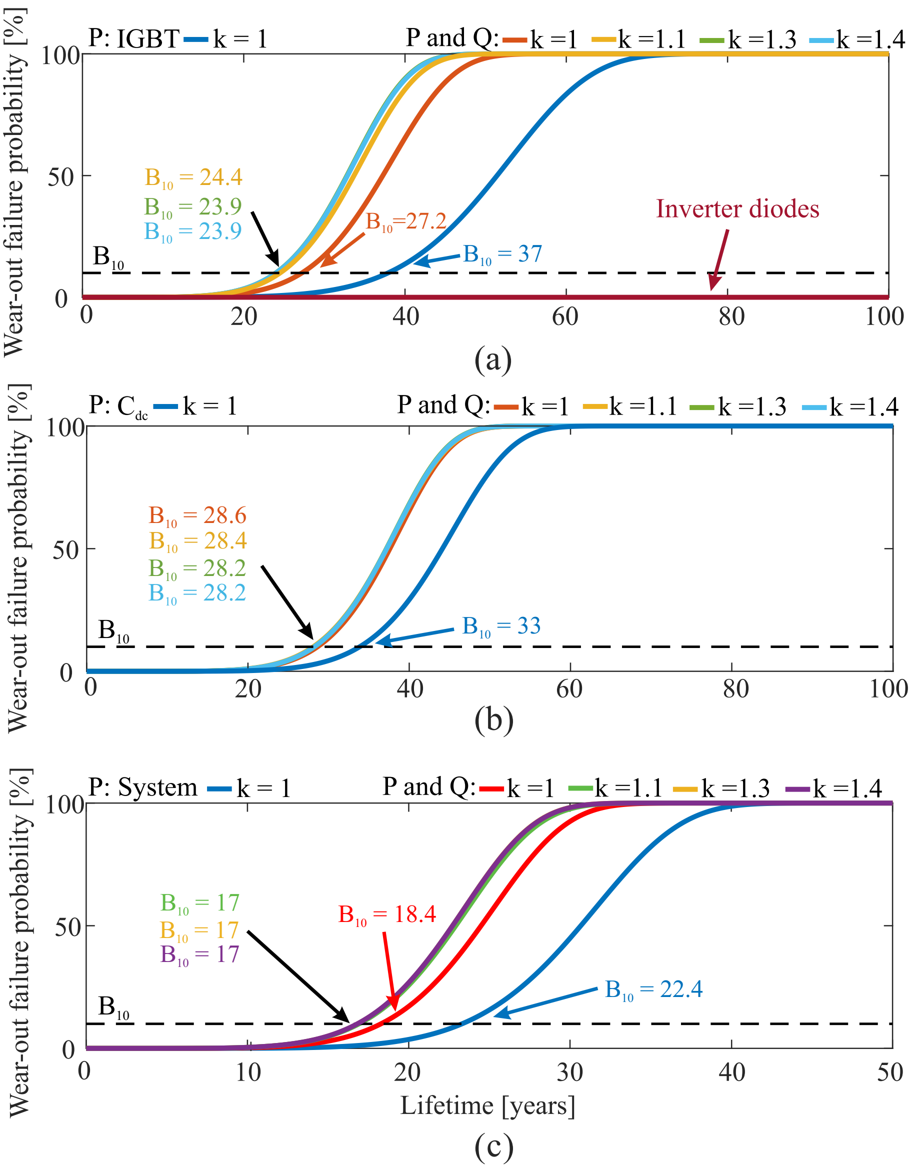

Figure 36 – PV inverter overload for different values of k: Unreliability curves of (a) semiconductors, (b) dc-link capacitors; (c) system. Monte Carlo simulations were performed considering a maximum variation of 10 % in ΔT_j and A, 2.5 % in T_{jm}, 20 % in L_0 and 15 % in T_h.

1200 V module (F3L100R12W2H3). Both of these IGBT modules share the same heatsink, since they have the same package. Moreover, a branch was added to the dc-link capacitor bank, i.e., the configuration changed from 5 branches containing 2 capacitors in series each (5x2) to the (6x2) configuration. For this analysis, the unreliability curves are shown in Fig. 37, considering $k = 1$ for all cases.

Fig. 37(a) and (b) show the component-level unreliability functions of the semiconductors and dc-link capacitors, respectively. In both cases, the oversizing of the components guarantees higher B_{10} reliability. Traditional inverter operation with semiconductors of 75 A and dc-link bank (5x2) is considered as the base case. The comparison between the base

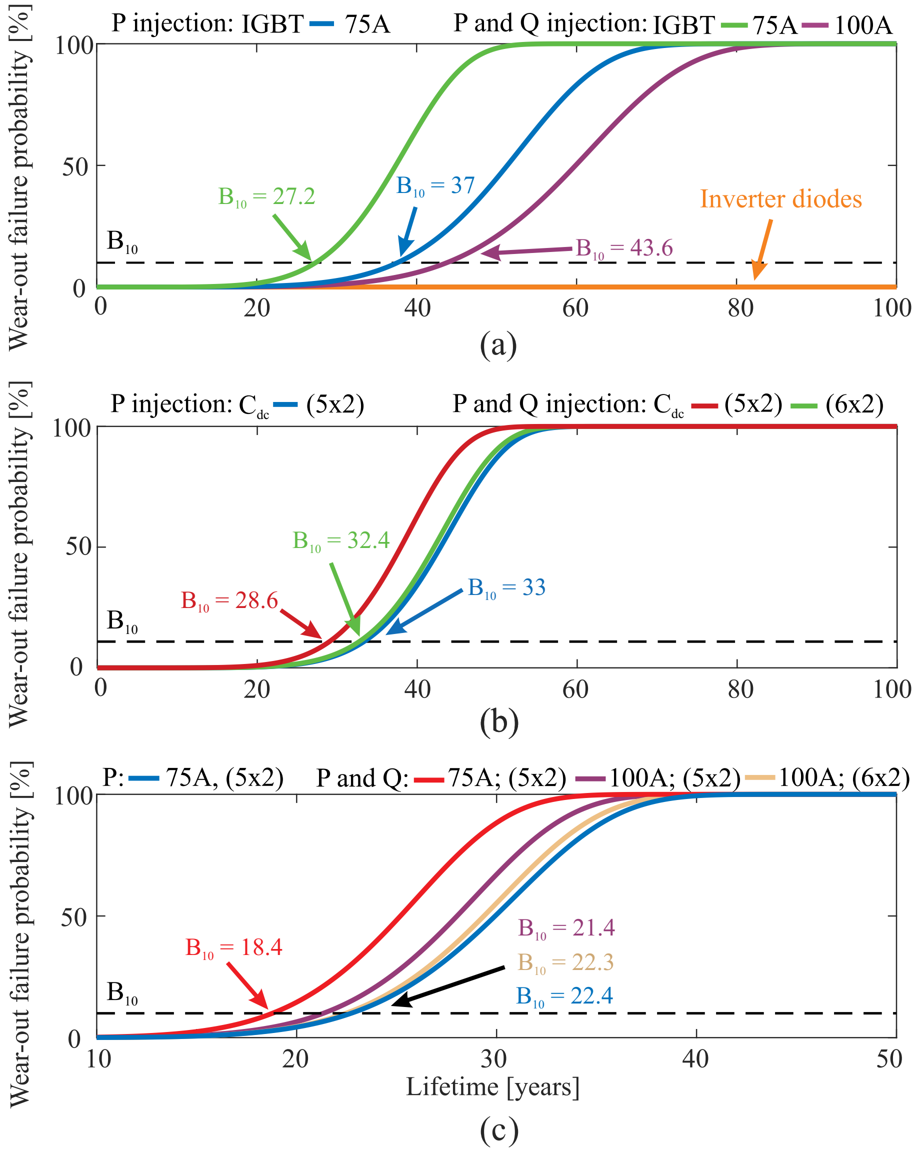

Figure 37 – PV inverter oversizing: Unreliability curves of (a) semiconductors, (b) dc-link capacitors; (c) system.

case and the multifunctional operation with 75 A and dc-link bank (5x2) reveals a 17.86 % reduction in the system reliability (from 22.4 to 18.4 years), as shown in Fig. 37(c). The B_{10} drops to below 20 years (base case target), considering the reactive power injection. When considering the oversizing of semiconductors from 75 A to 100 A while maintaining the same dc-link bank (5x2), the reduction in system reliability drops to 4.46 % (from 22.4 to 21.4 years), which satisfies the base case B_{10} target. Finally, the system reliability decreases 0.04 %, compared to the base case, considering the 100 A semiconductors and the dc-link bank (6x2) (from 22.4 to 22.3 years). This last result shows that multifunctional inverter oversizing allows to obtain almost the same base case reliability and to perform the PF correction, by means of reactive power injection.

5.4 Chapter Conclusions

The results detailed in this section show how the PF can be corrected effectively and the consequences on making this correction. The capacitor banks correct the average value to the reference specified and presents rippled correction. It is more interesting to fix this PF reference above the threshold to grant less trespassing and better correction. Also, different taps can achieve more combinations of capacitive power than using fixed taps optimizing the utilization of this method of correction.

Using a multifunctional PV inverter brings several advantages, since it corrects the PF with precision limited only by its rated power and does not demand the purchase of an expensive and complete capacitor bank. If its rated power is not enough for active power generation and correction, an oversizing will be needed. This oversizing of the inverter demands a more expensive PV inverter and increases the losses in the system. Over a research made in this work, it can be seen that this oversizing is not highly expensive and is still more viable than the capacitor.

Also, when the PV inverter is injecting reactive power, its injected current is higher and degrades its lifetime for about 5 years with the case study of this work. This is perceptible by the increase of the temperature on the components, which causes more degradation of the lifetime with slight increase in its value. The oversizing of the PV inverter increases the durability of the semiconductor devices and capacitors increasing again the total lifetime of the system. In fact, the optimum value of k increases its new lifetime to be the same it would be if it only injected active power.

Finally, these results bring the closure of this Master Thesis in the next chapter. The oversizing of the inverter show great advantage in substituting the capacitor bank on effective PF correction in industrial environments. In fact, the economy in the total investment is greatly increased when using the multifunctional PV inverter while maintaining the same total lifetime.

6 Closure

6.1 Conclusions

This work carried out a study on the effects of a PV plant on industrial companies. By generating local active energy to equal the consumed energy, the electricity bill presents the minimum value possible. However, there is a degrading effect on the power factor, which leads to low values. The power factor must be corrected in order to avoid fees over exceeding reactive power. This correction can be performed using either capacitor banks or the multifunctional inverter.

The tapped capacitor bank presented a traditional solution to correct the industrial power factor. Problems were observed mostly at the critical points ($P_{inv} = P_L$), which require an exact representation of the demanded curve. There is an extra cost for its implementation besides its greater volume. However, the capacitor bank does not demand the use of the inverter for reactive power compensation, which preserves the lifetime of the PV system. This can also create margin to use both equipments for power factor correction while preserving the lifetime for both.

The multifunctional inverter allows a suitable correction of the power factor while increasing the total investment. However, by compensating the reactive power, the inverter must process a higher level of current, which decreases its lifetime and increases power losses. Total reactive power compensation according to industry requirements reduces the system lifetime by 24.1 %, compared to traditional operation. However, the system reliability can be preserved by means of PV inverter oversizing. The cost increase of 14% due to the use of the inverter in the multifunctional mode was offset by the benefits.

6.2 Future Works

This work demonstrates a recent problem in PV plants installation, particularly in plants with high rated power. Since it is a new study over this topic, many future works can be done in order to research the effects of PV plants in the power factor. Future works might address:

- a more detailed economic analysis approach for this kind of investment;
- precise algorithms for reactive power prediction to calculate the capacitive power in real time;
- other control algorithms for the multifunctional PV inverter;

- an analytical estimation for the hotspot-to-ambient temperature for the capacitor in a PV inverter, since this topic lacks in the literature;
- the use of capacitor bank along with the multifunctional PV inverter, using the bank when the PV inverter alone cannot compensate the entire Q_C profile.

References

Absolar. *Infográfico Absolar*. 2020. 13, 27

Ahmed, M. R.; Alam, M. J. Power factor improvement by pulse width modulated switched single capacitor. In: *IICPE*. 2006. p. 212–215. 28

Andresen, M.; Ma, K.; Buticchi, G.; Falck, J.; Blaabjerg, F.; Liserre, M. Junction temperature control for more reliable power electronics. *IEEE Tran. Power Electron.*, p. 765–776, Jan 2018. 50

ANEEL. *Resolucao normativa nº 414/2010*. 2010. 27, 29, 60

Bhattacharya, K.; Zhong, J. Reactive power as an ancillary service. *IEEE Trans. Power Syst.*, v. 16, n. 2, p. 294–300, May 2001. 28

Callegari, J. M. S. *Lifetime Evaluation of Three-Phase Multifunctional PV Inverters with Reactive Power Compensation*. 2018. 13, 54

Callegari, J. M. S.; Cupertino, A. F.; Ferreira, V.; Pereira, H. A. Minimum dc-link voltage control for efficiency and reliability improvement in pv inverters. *IEEE Transactions on Power Electronics*, p. 1–1, 2020. 69

CanadianSolar. *Super High Power Poly Module - Datasheet*. 2018. 15, 59

Cupertino, A. F. *Modeling, Design and Fault-Tolerant Strategies for Modular Multilevel Cascaded Converter-based STATCOMs*. Tese (Doutorado) — UFMG, 11 2019. 13, 49

Cupertino, A. F.; Xavier, L. S.; Brito, E. M.; Mendes, V.; Pereira, H. A. Benchmarking of power control strategies for pv systems under unbalanced conditions. *Int. J. Elec. Power*, p. 335–345, 2019. 52, 61

EPCOS. *Aluminum electrolytic capacitors - Datasheet*. 2016. 61

Falck, J.; Felgemacher, C.; Rojko, A.; Liserre, M.; Zacharias, P. Reliability of power electronic systems: An industry perspective. *IEEE Ind. Electron. Mag.*, v. 12, n. 2, p. 24–35, June 2018. 54

Gandhi, O.; Rodríguez-Gallegos, C. D.; Gorla, N. B. Y.; Bieri, M.; Reindl, T.; Srinivasan, D. Reactive power cost from pv inverters considering inverter lifetime assessment. *IEEE Trans. Sustainable Energy*, v. 10, n. 2, p. 738–747, April 2019. 28

Gandhi, O.; Zhang, W.; Rodríguez-Gallegos, C. D.; Srinivasan, D.; Reindl, T. Continuous optimization of reactive power from pv and ev in distribution system. In: *ISGT-Asia*. 2016. p. 281–287. 28

Gomes, C. C.; Cupertino, A. F.; Pereira, H. A. Damping techniques for grid-connected voltage source converters based on lcl filter: An overview. *Renewable and Sustainable Energy Reviews*, v. 81, p. 116 – 135, 2018. ISSN 1364-0321. 35

Infineon. *FS75R12W2T4 IGBT Modules - Datasheet*. 2013. 61

Jafarian, H.; Cox, R.; Enslin, J. H.; Bhowmik, S.; Parkhideh, B. Decentralized active and reactive power control for an ac-stacked pv inverter with single member phase compensation. *IEEE Trans. on Industry Applications*, v. 54, n. 1, p. 345–355, Jan 2018. 28

JHMppe. *JHMppe*. 2020. Disponível em: <https://www.jhmppe.com.br/qbc>. 13, 35

Joksimovic, G. Transformer reactive power compensation–fixed capacitor bank calculation. *IEEE Trans. Power Delivery*, v. 30, n. 3, p. 1629–1630, June 2015. 28

Kekatos, V.; Wang, G.; Conejo, A. J.; Giannakis, G. B. Stochastic reactive power management in microgrids with renewables. *IEEE Trans. on Power Systems*, v. 30, n. 6, p. 3386–3395, Nov 2015. 28

Ko, W.; Gu, J.; Lee, W. Energy efficiency improvement of a single-phase ac spot welding machine by using an advanced thyristor switched detuning capacitor bank. *IEEE Trans. Ind. Appl.*, v. 54, n. 3, p. 1958–1965, May 2018. 28

Liu, L.; Li, H.; Xue, Y.; Liu, W. Reactive power compensation and optimization strategy for grid-interactive cascaded photovoltaic systems. *IEEE Trans. on Power Electron.*, v. 30, n. 1, p. 188–202, Jan 2015. 28

Lo, Y.; Lee, T.; Wu, K. Grid-connected photovoltaic system with power factor correction. *IEEE Trans. Ind. Electron.*, v. 55, n. 5, p. 2224–2227, May 2008. 28

Ma, K. *Power Electronics for the Next Generation Wind Turbine System*. 1. ed. : Springer International Publishing, 2015. ISBN 978-3-319-21247-0. 51

Ma, K.; Blaabjerg, F. Reliability-cost models for the power switching devices of wind power converters. In: *IEEE PEDG*. 2012. p. 820–827. 51

Masters, G. M. *Renewable and Efficient Electric Power Systems*. Hoboken, New Jersey: John Wiley Sons, Inc, 2004. 40

McPherson, J. W. *Reliability Physics and Engineering: Time-to-Failure Modeling*. 2010. 49

Moore, L. M.; Post, H. N. Five years of operating experience at a large, utility-scale photovoltaic generating plant. *Progress in Photovoltaics: Research and Applications*, v. 16, n. 3, p. 249–259, 2008. 28

Morales-Paredes, H. K.; Bonaldo, J. P.; Pomilio, J. A. Centralized control center implementation for synergistic operation of distributed multifunctional single-phase grid-tie inverters in a microgrid. *IEEE Trans. Ind. Electron.*, v. 65, n. 10, p. 8018–8029, Oct 2018. 28

Peña-Alzola, R.; Liserre, M.; Blaabjerg, F.; Ordonez, M.; Yang, Y. Lcl-filter design for robust active damping in grid-connected converters. *IEEE Transactions on Industrial Informatics*, v. 10, n. 4, p. 2192–2203, Nov 2014. ISSN 1551-3203. 36

Pereira, H. A.; Domingos, R. M.; Xavier, L. S.; Cupertino, A. F.; Mendes, V. F.; Paulino, J. O. S. Adaptive saturation for a multifunctional three-phase photovoltaic inverter. In: *ECCE-Europe*. 2015. p. 1–10. 36

phbSolar. *Inversor Solar Fotovoltaico Trifásico Certificado pelo INMETRO - Datasheet*. 2016. 59

Prasai, A.; Divan, D. M. Control of dynamic capacitor. *IEEE Trans. Ind. Appl.*, v. 47, n. 1, p. 161–168, Jan 2011. 28

Prasai, A.; Sastry, J.; Divan, D. M. Dynamic capacitor (d-cap): An integrated approach to reactive and harmonic compensation. *IEEE Trans. Ind. Appl.*, v. 46, n. 6, p. 2518–2525, Nov 2010. 28

Reigosa, P. *Smart Derating of Switching Devices for Designing More Reliable PV Inverters.* Dissertação (Mestrado) — Aalborg University, 2014. 50

Reigosa, P.; Wang, H.; Yang, Y.; Blaabjerg, F. Prediction of bond wire fatigue of igbts in a pv inverter under a long-term operation. *IEEE Transactions on Power Electronics*, v. 31, n. 10, p. 7171–7182, 2016. 47, 54

Ribeiro, G. A. G.; Antônio, A. d. S.; Moreira, T. M. S.; Martins, G.; Pereira, H. A. Development of a sun tracker. In: *IEEE ISGT*. 2013. p. 1–6. 40

Rodríguez, P.; Teodorescu, R.; Candela, I.; Timbus, A. V.; Liserre, M.; Blaabjerg, F. New positive-sequence voltage detector for grid synchronization of power converters under faulty grid conditions. p. 1–7, 2006. 36

Sangwongwanich, A.; Yang, Y.; Sera, D.; Blaabjerg, F. Lifetime evaluation of grid-connected pv inverters considering panel degradation rates and installation sites. *IEEE Trans. Power Electron.*, p. 1225–1236, Feb 2018. 54

Sangwongwanich, A.; Yang, Y.; Sera, D.; Blaabjerg, F. Mission profile-oriented control for reliability and lifetime of photovoltaic inverters. In: *ECCE Asia*. 2018. 53

Scheuermann, U.; Schmidt, R.; Newman, P. Power cycling testing with different load pulse durations. In: *PEMD*. 2014. p. 1–6. 53

Sousa, C. V. de. *Projeto e Montagem de uma Bancada Regenerativa para Ensaios de Carregamento em Transformadores de Potência*. Tese (Doutorado) — UFMG, 12 2011. 37

Su, X.; Masoum, M. A. S.; Wolfs, P. J. Optimal pv inverter reactive power control and real power curtailment to improve performance of unbalanced four-wire lv distribution networks. *IEEE Trans. Sustainable Energy*, v. 5, n. 3, p. 967–977, July 2014. 28

Vernica, I.; Wang, H.; Blaabjerg, F. Uncertainty analysis of capacitor reliability prediction due to uneven thermal loading in photovoltaic applications. *Microelectron. Reliab.*, v. 88-90, p. 1036 – 1041, 2018. Esref 2018. 50

Villalva, M. G.; Gazoli, J. R.; Filho, E. R. Comprehensive approach to modeling and simulation of photovoltaic arrays. *IEEE Trans. Power Electron.*, v. 24, n. 5, p. 1198–1208, May 2009. 50

Wandhare, R. G.; Agarwal, V. Reactive power capacity enhancement of a pv-grid system to increase pv penetration level in smart grid scenario. *IEEE Trans. Smart Grid*, v. 5, n. 4, p. 1845–1854, July 2014. 27

Wang, H.; Davari, P.; Wang, H.; Kumar, D.; Zare, F.; Blaabjerg, F. Lifetime estimation of dc-link capacitors in adjustable speed drives under grid voltage unbalances. *IEEE Tran. Power Electron.*, v. 34, n. 5, p. 4064–4078, May 2019. 51

Wang, H.; Liserre, M.; Blaabjerg, F.; de Place Rimmen, P.; Jacobsen, J. B.; Kvisgaard, T.; Landkildehus, J. Transitioning to physics-of-failure as a reliability driver in power electronics. *IEEE J. Emerg. Sel. Topics Power Electron.*, March 2014. 49, 50

Weckx, S.; Gonzalez, C.; Driesen, J. Combined central and local active and reactive power control of pv inverters. *IEEE Trans. Sustainable Energy*, v. 5, n. 3, p. 776–784, July 2014. 28

WGR Ignitron. *WGR*. 2020. Disponível em: <http://www.wgr.com.br/banco-capacitor-fixo>. 13, 34

Wolfgang, E. Examples for failures in power electronics systems. *Proc. Tuts. Rel. Power Electron. Syst.*, 2007. 47, 49

Xavier, L. S.; Cupertino, A. F.; Pereira, H. A. Ancillary services provided by photovoltaic inverters: Single and three phase control strategies. *Computers & Electrical Engineering*, v. 70, p. 102 – 121, 2018. 37

Yang, S.; Bryant, A.; Mawby, P.; Xiang, D.; Ran, L.; Tavner, P. An industry-based survey of reliability in power electronic converters. *IEEE Transactions on Industry Applications*, v. 47, n. 3, p. 1441–1451, 2011. 13, 48

Yang, Y.; Sangwongwanich, A.; Blaabjerg, F. Design for reliability of power electronics for grid-connected photovoltaic systems. *CPSS Trans. Power Electron. and Appl.*, v. 1, n. 1, p. 92–103, Dec 2016. 27

Ye, T.; Dai, N.; Lam, C.; Wong, M.; Guerrero, J. M. Analysis, design, and implementation of a quasi-proportional-resonant controller for a multifunctional capacitive-coupling grid-connected inverter. *IEEE Trans. Ind. Appl.*, v. 52, n. 5, p. 4269–4280, Sept 2016. 28

Biography

Lucas Soares Gusman was born in Muriaé/MG, Brazil in 1996. He obtained the B.S. degree in Electrical Engineering from the Universidade Federal de Viçosa (UFV), in Viçosa/MG, Brazil in 2019. In this institution, he carried out researches in the Gerência de Especialistas em Eletrônica de Potência (GESEP). Currently, he is a Senior Researcher at GESEP, in the area of Power Electronics and Photovoltaic Energy, actuating on the study of power factor correction through multifunctional PV inverters.

E-mail: lucasgusman@yahoo.com.br